



**Politecnico  
di Torino**

## **POLITECNICO DI TORINO**

Corso di Laurea Magistrale in Automotive Engineering

Tesi di Laurea Magistrale

# **Design of an origami shaped composite structure with application to a race car crash absorber**

**Supervisor:**

Prof. Davide Salvatore Paolino

**Co-Supervisor:**

Prof. Alberto Ciampaglia

Prof. Raffaele Ciardiello

Prof. Dario Fiumarella

**Candidate:**

Luca Patruno s300110

Academic Year 2022–2023



*Alla mia famiglia*



# Abstract

The thesis, with title *“Design of an origami shaped composite structure with application to a race car crash absorber”*, focuses on the design of an origami-shaped composite structure for use in a race car crash absorber. The goal of the crash box is to guarantee progressive and controlled energy absorption, avoiding peak force that can lead to passenger injury. The origami structure is increasingly considered for crash boxes due to its ability to improve the crashing behavior of composite material structures by modifying their geometrical parameters. The work is focused on design, production, and test of a CFRP crash box that will be compliant with the Formula Student rules using a reliable numerical model validated through real tests. Preliminary characterization of the used material has been investigated; in addition, to fit the numerical model, seven specimens were crashed to have correct experimental feedback. Such research was conducted thanks to the support of Squadra Corse PoliTo; Centro Sicurezza Stellantis Group and Dipartimento di Meccanica Politecnico di Torino. The results showed that the designed crash box was able to meet the requirements of Formula Student rules and provided good energy absorption performance. In conclusion, work demonstrates the potential of origami structures for improving the crashing behavior of composite material structures and provides valuable insights for future research in this field.



# Contents

<b>1</b>	<b>Introduction</b>	<b>1</b>
1.1	Motivation . . . . .	1
1.2	Work Objective . . . . .	1
<b>2</b>	<b>Formula SAE and requirements</b>	<b>3</b>
2.1	Acronyms . . . . .	3
2.2	Formula SAE rules . . . . .	4
2.2.1	Safety rules . . . . .	4
2.2.2	Impact Attenuator . . . . .	5
2.3	IA requirements . . . . .	6
2.3.1	IA Geometrical Needs . . . . .	6
2.3.2	IA Test Requirements . . . . .	7
2.3.3	Limits Force Requirements . . . . .	9
2.3.4	Facility Requirements . . . . .	9
<b>3</b>	<b>State of the art</b>	<b>11</b>
3.1	Carbon Fiber Crashbox . . . . .	11
3.2	Approaches to Numerical Modelling . . . . .	12
3.3	CFRP Failure Modes . . . . .	13
3.3.1	MODE I . . . . .	13
3.3.2	MODE II . . . . .	14
3.3.3	MODE III . . . . .	15

3.4	Shell and Cohesive Approaches . . . . .	15
3.4.1	Shell Modelling . . . . .	15
3.4.2	Cohesive Zone Modelling . . . . .	16
3.5	Crashworthiness test . . . . .	17
3.6	State-of-the-Art consideration . . . . .	18
<b>4</b>	<b>Material Characterization</b>	<b>19</b>
4.1	Carbon Fiber Material: T300 . . . . .	19
4.2	Matrix Epoxy Resin: DT806W . . . . .	20
4.3	Tensile Test Characterization . . . . .	21
4.3.1	Specimen production . . . . .	21
4.3.2	Tensile Test Procedure . . . . .	23
4.4	Compression Test Characterization . . . . .	24
4.4.1	Specimen production . . . . .	24
4.4.2	Compression Test Procedure . . . . .	26
4.5	Material post process data . . . . .	29
4.6	Material Card . . . . .	31
4.6.1	MAT 054 . . . . .	31
4.6.2	MAT 54 PARAMETER . . . . .	33
4.6.3	MAT 138 . . . . .	34
4.6.4	MAT 138 PARAMETER . . . . .	36
<b>5</b>	<b>Impact Attenuator Desing and Production</b>	<b>37</b>
5.1	Origami Shape . . . . .	37
5.2	Geometry Design . . . . .	38
5.2.1	Geometry . . . . .	39
5.3	IA Specimen Production . . . . .	40
5.3.1	WB 700 epoxy mould . . . . .	40
5.3.2	Al mould . . . . .	42

5.3.3	Hand Layup Specimen Lamination . . . . .	43
5.3.4	Specimen notation . . . . .	46
<b>6</b>	<b>Experimental Test</b>	<b>49</b>
6.1	Test Rig . . . . .	49
6.2	Specimen Data . . . . .	51
6.3	Acquired data . . . . .	51
6.4	Post process . . . . .	52
6.4.1	Data post process . . . . .	53
6.4.2	Video Post process . . . . .	55
6.5	Post process result and conclusions . . . . .	57
6.5.1	Breakup Dynamics . . . . .	58
6.5.2	Acceptability bounds . . . . .	60
<b>7</b>	<b>Numerical Model</b>	<b>63</b>
7.1	Mesh . . . . .	63
7.2	Trigger mesh element . . . . .	64
7.3	Shell Model . . . . .	67
7.4	Combined Model (Shell+Cohesive) . . . . .	68
7.4.1	Cohesive element implementation . . . . .	68
7.5	Boundary Conditions . . . . .	69
7.6	FEM results . . . . .	70
7.6.1	Force displacement curve - shell model . . . . .	70
7.6.2	Force displacement curve - combined model . . . . .	71
7.6.3	Numerical model error . . . . .	72
7.6.4	crash behaviour . . . . .	75
<b>8</b>	<b>IA final configuration</b>	<b>79</b>
8.1	Final layup . . . . .	79
8.2	Force displacement curve . . . . .	80

8.3 Performances indicator and comparison with previous attenuator . . . . . 82

**9 Conclusions** **85**



# List of Figures

2.1	Politecnico di Torino FSAE car (year 2022-2023)	4
2.2	Monocoque and Impact Attenuator Assembly	5
2.3	Fixture front side and rear one	8
3.1	Micro, meso and macro scale modelling approaches	13
3.2	Lack of resin effect during traction test characterization	14
3.3	Cohesive element between carbon fiber shell plies	16
4.1	Woven Fabric 2×2 twill 3k	20
4.2	DT806 Temperature Viscosity Profile	21
4.3	Tensile Specimen-before the test	23
4.4	Tensile Specimen – after the test	24
4.5	Test fixture for compression characterization	26
4.6	Overall Caption for the Image Block	28
4.7	Mechanical tensile/compression curve	30
4.8	MAT 138 – Constitutive model	34
4.9	MAT 138 – Mixed Mode	35
5.1	Characteristic origami crash box angles	37
5.2	Single origami structure model	38
5.3	Single module dimension	39
5.4	Single crash box dimension	40
5.5	Epoxy resin mould – WB 700	41
5.6	Aluminium mould	42

5.7	3 modules plies . . . . .	43
5.8	2 modules plies . . . . .	43
5.9	1 modules plies . . . . .	43
5.10	Production methods: Strip and Overlap . . . . .	44
5.11	Overlap criteria . . . . .	45
5.12	Impact validation specimen . . . . .	46
5.13	Production photos . . . . .	48
6.1	sled hammer scheme . . . . .	50
6.2	Post process block diagram . . . . .	52
6.3	Sensors data processing . . . . .	53
6.4	Force and acceleration signals . . . . .	54
6.5	Specimen before impact . . . . .	55
6.6	Tracked points-video post process . . . . .	55
6.7	Velocity comparison . . . . .	56
6.8	Specimen displacement . . . . .	57
6.9	Force-displacement curves . . . . .	57
6.10	Iso-energetic tested specimen force-displacement curves . . . . .	58
6.11	10262_C_05(S)-crash frames . . . . .	59
6.12	Validation acceptability bounds . . . . .	61
6.13	Standard deviation candle plot . . . . .	62
7.1	Quarter crash box mesh . . . . .	64
7.2	First failure point - crash box . . . . .	65
7.3	Kinematic drape output . . . . .	66
7.4	First failure point - crash box . . . . .	67
7.5	Cohesive implementation . . . . .	69
7.6	Combined model . . . . .	69
7.7	Force displacement curve - shell model . . . . .	70

7.8 Force displacement curve - combined model . . . . .	71
7.9 Energy absorption . . . . .	73
7.10 Characteristic points . . . . .	74
7.11 crash frames numerical model . . . . .	75
7.12 Delamination frames numerical model . . . . .	76
7.13 Force displacement interpretation . . . . .	76
8.1 Target FEM model-half structure . . . . .	81
8.2 force displacement curve - final setup . . . . .	81
8.3 Previous attenuator structure . . . . .	82
8.4 Performances comparison - old and new attenuator structure . . . . .	83



# List of Tables

4.1	Tensile specimen layup . . . . .	22
4.2	Tensile specimen dimension . . . . .	22
4.3	Tensile specimen layup . . . . .	25
4.4	Compression specimen dimension . . . . .	25
4.5	Material Properties . . . . .	31
4.6	MAT 54 input data . . . . .	33
4.7	MAT 138 input data . . . . .	36
5.1	Layup validation specimens . . . . .	45
6.1	Specimen Test Condition . . . . .	51
6.2	Acquisition sensor parameter . . . . .	52
7.1	Mesh quality index components . . . . .	65
7.2	Cohesive thickness . . . . .	68
7.3	Numerical model performances . . . . .	72
7.4	Max and mean acc. comparison . . . . .	73
7.5	Force numerical values - characteristic points . . . . .	74
7.6	Specific Energy Absorption for each crash box module . . . . .	75
8.1	Old and new attenuator performances . . . . .	83





# Chapter 1

## Introduction

### 1.1 Motivation

In order to reduce the severity and avoid fatalities in case of crash event, passive safety systems are necessary; especially in the automotive field, minimizing the transmitted force to the occupants and avoiding serious injuries. The increasing of the safety requirements lead to a more advanced system. Carbon fiber is a material that has been used in the motorsport world, primarily for its lightweight and high-strength properties. This, in turn, can help to reduce the overall weight of the vehicles, the emission, and increasing the fuel economy. However, there are also some drawbacks related to this material: the design phase and the production one are so expensive and not ready for big scale scenario. Despite these challenges, the carbon fiber is still considered an alternative and promising solution for the next future of the occupant's safety.

### 1.2 Work Objective

The goal of the crash box is to guarantee progressive and controlled energy absorption, avoiding peak force that can lead to passenger injury. The origami structure is increasingly considered for crash boxes due to its ability to improve the crashing behavior of composite material structures by modifying their geometrical parameters.

Work is focused on design, production, and test of a CFRP crash box, that will be compli-

ant with the Formula Student rules, using a reliable numerical model, validated through real tests. The crash box has a preformed origami shape, primarily studied in [1]. Preliminary characterization of the used material has been investigated; in addition, to fit the numerical model, seven specimens were crashed to have a correct experimental feedback. Such research was conducted thanks to the support of the Centro Sicurezza, Stellantis group; Squadra Corse PoliTo and Dipartimento di Meccanica Politecnico di Torino. The system should have the main purpose of protecting the driver in case of a frontal crash, minimizing the transmitted force during the event. Instead, the numerical model will help in the next future to study other suitable devices using the carbon fiber material.

# Chapter 2

## Formula SAE and requirements

The Formula SAE is an international competition held by university student coming from all over the world. Born in the 1981 thanks to Society of Automotive Engineer, the formula SAE experience shares the philosophy “learning by doing”, giving the opportunity to put in practice the learned knowledges.

### 2.1 Acronyms

In the following, for sake of clarity, the acronyms useful to proceed in the treatment:

- **AIP:** Anti Intrusion Plate
- **CFRP:** Carbon Fiber Reinforcement Polymers
- **FBH:** front Bulkhead
- **IA:** Impact Attenuator
- **IAD:** Impact Attenuator Documentation
- **SES:** Structural Equivalency Spreadsheet

## 2.2 Formula SAE rules

### 2.2.1 Safety rules

Formula SAE competition share every year the updated rules. These are mandatory in order to participate in the dynamics events of the competition. Majority ones are related to the chassis environment, in the case of Politecnico di Torino FSAE car the chassis are realized in CFRP.



*Figure 2.1: Politecnico di Torino FSAE car (year 2022-2023)*

To be compliant with the rules, must be carried out experimental test to show, in real scenario, the performances of the laminated structure of the vehicles, demonstrating the equivalency with two steel tubes with a case load of tree-point bending. In addition, particular attention, for safety reason, is shown to the passive safety systems called **Impact Attenuator**: a structure that must be capable to absorb the right amount of energy in case of frontal crash event.

### 2.2.2 Impact Attenuator

The passive systems play one of the most important roles in the vehicles occupant's safety, minimizing the transmitted force during a crash event and avoiding injuries. In the Formula SAE world, the **impact attenuator** is in charge of absorbing the energy in case of a longitudinal crash.

Every Formula SAE vehicle must be equipped with an impact attenuator **IA**. Each team is free to choose the "standard" structure, already designed by the customer, or in alternative, try to design and develop it independently. In this latter case, the structure must be tested in a real test and the data are not processed by a student member, but by the certified centre emitting the document.

In the next picture will be presented the impact attenuator assembly to have a clear understanding of the component and functionalities.

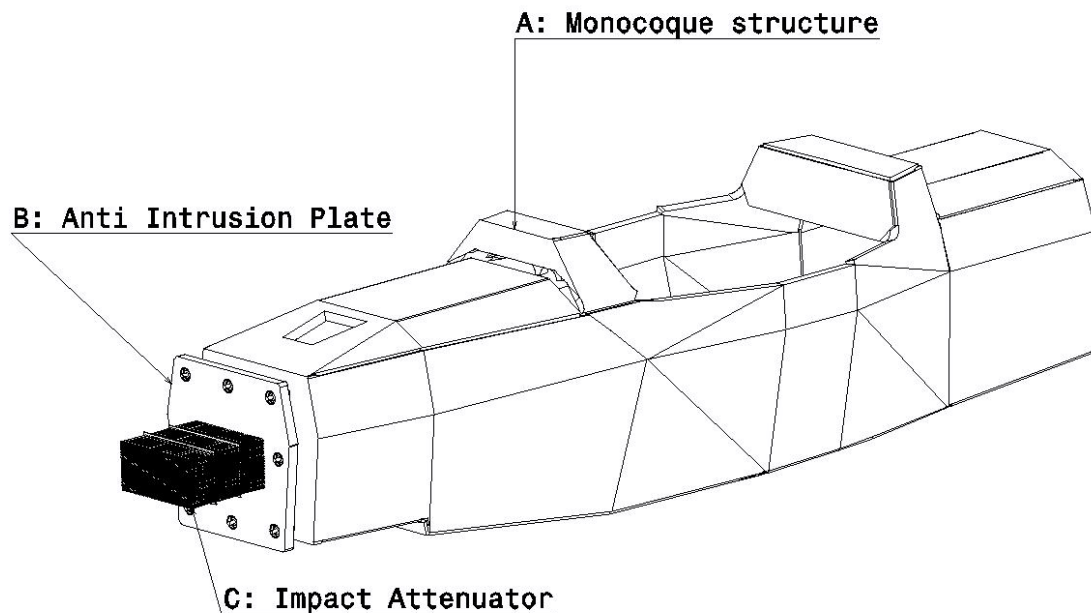


Figure 2.2: Monocoque and Impact Attenuator Assembly

In the above figure 2.2, it is presented the monocoque and the impact attenuator assembly. The car structure is realized in a sandwich configuration panel, composed by honeycomb and prepreg plies of CFRP. The impact attenuator, in the picture element C, is attached to the Anti Intrusion Plate **AIP**; this last one is attached through 9 screws grade 8.8 steel coming out from the monocoque. Also, the AIP is, in our case, realized in hybrid structure. It is important to mention, that the depicted assembly is referred to the old version of the impact structure. The scope of the thesis work is to substitute the old honeycomb impact structure with one realized in carbon fiber.

In the monocoque, the carbon fiber layup is not the same for all the zones; in the design phase, it is useful to define the layup zones following structural requirements. The area where the AIP interfaces is called FHB, front bulk head.

### **2.3 IA requirements**

The Impact Attenuator structure have several geometrical, energetical and positioning requirements.

The requirements depend on choose from the team to adopt or not the standard IA structure or developed it in other way. Regulation permits alternative IA as well as AIP. As mentioned in the official documents, the IA requirements are listed in the section T 3.17 of the FS rules 2023 v1.1 [2]

#### **2.3.1 IA Geometrical Needs**

- Each vehicle must be equipped with an IA.
- Installed forward of the front bulkhead.
- At least 100 mm high and 200 mm wide for a minimum distance of 200 mm forward of the front bulkhead.

- No portion of the required  $100 \times 200 \times 200$  mm<sup>3</sup> volume of the IA can be positioned more than 350 mm above the ground.
- Not able to penetrate the front bulkhead in the event of an impact.
- Attached securely and directly to the AIP.
- Not part of the non-structural bodywork.
- Designed with a closed front section.
- Cannot be wider or higher than the AIP.
- Alternative AIP designs are permissible if equivalency to T 3.17.3 is proven by physical testing, as in T 3.19.2.

### **2.3.2 IA Test Requirements**

The test will be performed using a not yielding barrier with a mass of 300 kg moving at 7 m/s. The mass of 300 kg is representative of the car weight because it is not the effective real weigh. Generally, the FSAE car weights less than this mass, so the rules are in favour of safety.

To simulate the monocoque and not make the experimental assembly test too hard to realize, a fixture will be used. When alternative materials are used for the AIP, in our particular case the CFRP, the test fixture must be a copy of the intended primary structure. The layup of the fixture is the same as the monocoque structure.

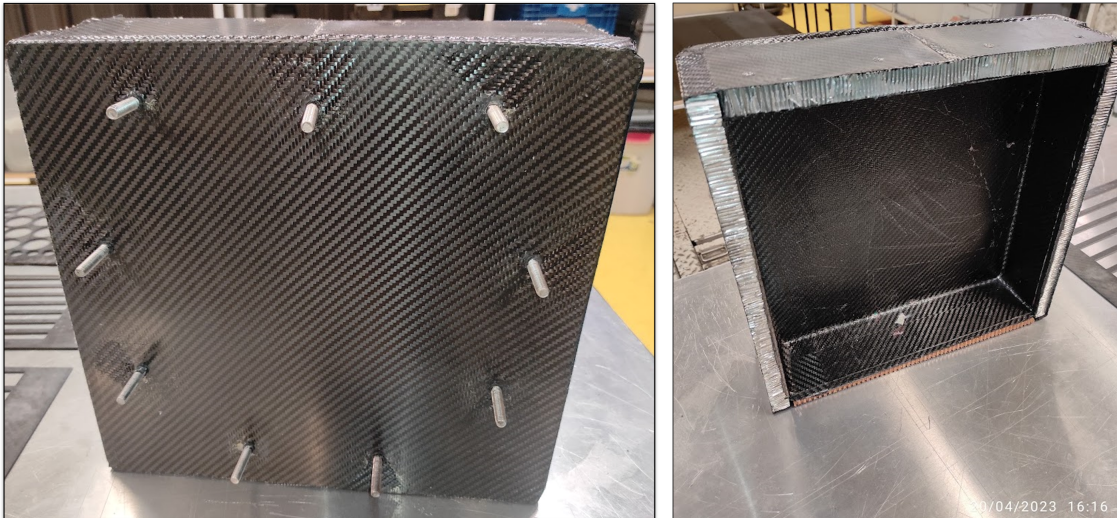


*Figure 2.3: Fixture front side and rear one*

During the test, the structure must meet the requirements [2]:

- Decelerate the vehicle at a rate not exceeding 20 g average and 40 g peak.
- The energy absorbed in this event must meet or exceed 7350 J.

Instead, for the attachments method the following ones must be satisfied:

- The IA must be attached to the AIP using the intended vehicle attachment method.
- The IA assembly must be attached to a test fixture that has geometry representative of the intended primary structure and equal or higher stiffness and strength.
- When alternative materials are used for the AIP, the test fixture must be a copy of the intended primary structure (i.e. materials, lay-up, joining methods).
- There must be at least 50 mm clearance rearwards of the AIP to the test fixture.
- No part of the AIP may permanently deflect more than 25 mm beyond the position of the AIP before the test.

As it is possible to see in figure 2.3 in front position, the fixture have 9 special inserts fully laminated in the AIP panel. In the rear side are visible the different thickness of the honeycomb due to the presence of the floor panel with a 10 mm honeycomb thickness. Clearly the layup used to realize the fixture is the one used for the monocoque, to fulfil the rules.

### 2.3.3 Limits Force Requirements

In case of aerodynamics, components and devices in front of the FBH. It must be proved that the total force contribution coming from the IA assembly physical testing and the shear force of the fastener screws of non-crushable objects does not exceed the value of 120 kN. To summarize, the relation is:

$$F_{IA} + F_{Screw} \leq 120kN \quad (2.1)$$

### 2.3.4 Facility Requirements

The physical test must be performed by dedicated test facilities. The students are not allowed to design the crash apparatus.

Finally, raw unfiltered data will be used to calculate the average deceleration, less or equal to 20g. If deceleration peaks above 40g are present, a low pass Butterworth (-3dB at 100Hz) filter may be used.



# Chapter 3

## State of the art

In the field of car safety crash, the passive systems are in charge to absorb the kinetic energy, attenuating the transmitted force to the cockpit where the occupants are. For what concern the origami shape a specific paper, et al. [1], discusses an investigation into the crash response of a CFRP origami crash box subjected to axial impact. The result shown that more inclined faces in the top part can guarantee a fracture-triggering effect in the crash box, which ensured a smaller peak force. The optimized origami crash box presents enhanced properties with respect to a conventional squared section crash box, in terms of crash efficiency. This confirmed the possibility to tune the crash and impact properties of a crash box by modifying its geometry without affecting the mass. The proposed work sees an unusual approach in the crash box FSAE Impact attenuator with respect to literature [3], for which the tapered shape is preferred in order to have a linear progression of the plies. Still, a short digression on origami shape is carried out in the next section.

### 3.1 Carbon Fiber Crashbox

An interesting analysis, carried out in [4], on the design and experimental verification of a composite impact attenuator for racing FSAE vehicles. The researchers performed a preliminary design of an impact attenuator based on the energy absorption character-

istics of composites, competition rules, and overall vehicle arrangement. Using LS-OPT software and verified through quasi-static axial compression and dynamic drop-weight impact tests, the design was optimized.

The research article about the lightweight design and crash analysis of composite frontal impact energy absorbing structures [5] discuss the use of carbon fiber composites in energy-absorbing components for motorsports and aerospace engineering. They present the steps to design a specific lightweight impact attenuator using mathematical formulation, pointing out a work equation needed to bend, fracture, braking fibers and matrix, as well as experimental dynamic tests using a drop weight test machine. The authors also discuss the design of a composite nose cone for a Formula SAE racing car, including quasi-static testing and numerical simulation of dynamic stroke.

### 3.2 Approaches to Numerical Modelling

The numerical modelling follows the length scale of the events. The carbon fiber reinforcement polymers, in general, have three failure mode, called in literature **MODE I**, **MODE II** and **MODE III**. In order to catch all the three method, several approaches are available on the market trough FEM Software. Based, also, on the level of details of the problem we can have MICROSCALE, MESOSCALE or MACROSCALE. The first one sees the interaction between each fiber surrounded by matrix. For the second method approach, the carbon fiber is seen like a shell kept together by a solid matrix element. Instead, for the latter case only the carbon fiber interaction is highlight, so the matrix is lost, and the plies are modelled in shell elements. In this work, the mesoscale and macro ones will be compared. Clearly, increasing the level of detail of the event is proportional to the computational power needed.

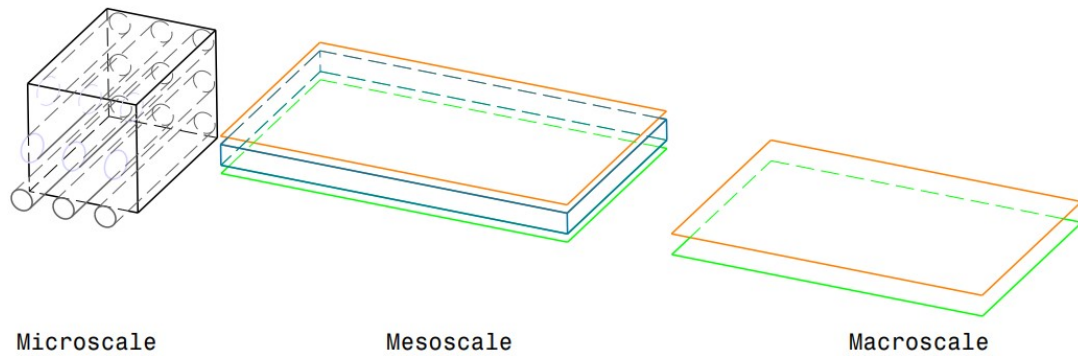


Figure 3.1: Micro, meso and macro scale modelling approaches

### 3.3 CFRP Failure Modes

Carbon fiber is a composites material known for high stiffness with respect to weight. It consists of carbon fibers embedded in a polymer matrix, in our case epoxy resin. Different fiber orientation determines mechanical properties along each direction, this is known in material science *anisotropy*. For what concern the failure mode and the fracture behaviour of the carbon fiber composites, in literature, three modes are considered: **MODE I**, **MODE II**, **MODE III**. In the following will be shortly analysed each single mode.

#### 3.3.1 MODE I

Also called *Opening Mode* or *Tensile fracture*, occurs when a crack propagates along the applied stress direction, and it continues separating the material along the fracture plane. This type of fracture is approachable when the structure is subjected to a tensile load.

As say before the CFRP is an anisotropy material, in this case the fibers carry most of the load. By the fibers braking, the crack propagates. Although the fiber have better mechanical properties with respect to matrix, this is essential, because is in charge to direct correct the load along the fibers. If in the same areas the matrix is

not present, the fibers will be disoriented and not able to support the load, resulting in fibers disarray effect.

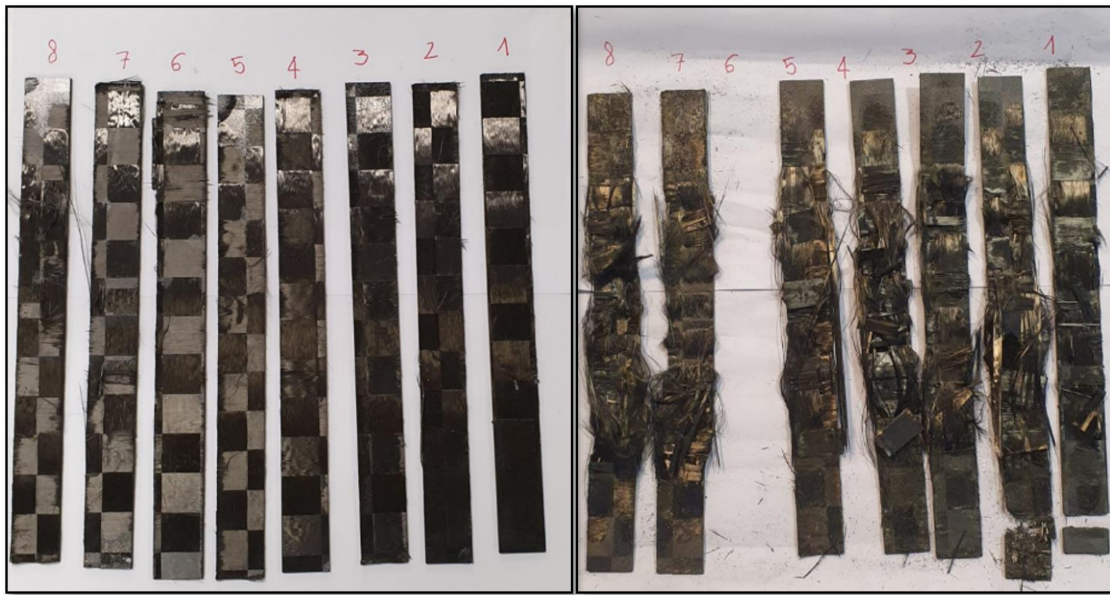


*Figure 3.2: Lack of resin effect during traction test characterization*

In the above figure 3.2 are presented eight specimens for traction characterization, following the ASTM 3039 standard.

The used carbon fiber is Textreme and was not used in the production phase of IAs, but it is useful to understand the essential purpose of the resin; in fact the matrix is in charge of correctly distribute the load along the fiber direction. In this case, the lack of resin leads, during traction load, disarrays all the fibers.

### **3.3.2 MODE II**

Mode II fracture is an in-plane shear fracture, because the crack propagates parallel to the plane of applied shear stress. This mode of fracture is relevant when considering structures subjected to shear loads, such as inter laminar shear stress.

In Mode II, the fibers and the matrix slide past each other along the crack plane, leading to propagate. The fracture toughness in this mode is influenced by the interfacial

properties between the fibers and the matrix, including adhesion shear strength.

### **3.3.3 MODE III**

Mode III fracture, occurs in the orthogonal direction of the MODE II, crack propagates perpendicular to the plane of shear stress applied. This mode of fracture is less common. In Mode III, the crack propagates by tearing the material along the shear plane. The carbon fibers play a less significant role in Mode III compared to Modes I and II, as the fracture primarily involves the behavior of the polymer matrix. The fracture toughness in Mode III depends on the resistance to shear deformation and the energy required to tear the material apart.

## **3.4 Shell and Cohesive Approaches**

In the proposed work will be analysed two approaches, for what concern the modelling FEM model, using Ls-Dyna software.

The following material card were being utilized in the model:

- MAT 054-055: MAT ENHANCED COMPOSITE DAMAGE
- MAT 138: MAT COHESIVE MIXED MODE

### **3.4.1 Shell Modelling**

According to [1], the Finite Element Model, in this case, of the origami crash box, can follow a shell modelling approach. Using Ls-Dyna, the model follows Belytschko Tsai 4 node shell elements with six degrees of freedom per node were used to model the structure, with a mesh size of 5 mm. The material model used was the (MAT 54/55), simulating the carbon fiber plies as shell. The material properties considered for the material card were obtained from experimental tests. The non-physical parameter SOFT of the material card MAT 54/55 was assessed and set by means of a trial and

error process, comparing simulation with experimental results. Two triggers were also modelled in correspondence of the upper and lower row of elements to simulate imperfections and weakening of the component's edges generated during the cutting phase. The Young's moduli and strain to failure in the longitudinal direction were changed to limit the peak force of the first contact with the rigid wall.

### 3.4.2 Cohesive Zone Modelling

For what concern the Cohesive approach, we want to simulate the interface between the carbon fiber plies and the matrix layer in between, in [6], authors discuss the use of cohesive zone modelling **CMZ** as an efficient technique for modelling adhesively bonded interfaces in structure-level simulations. The authors conducted a parametric study to examine the effect of cohesive element formulation, adherent element selection, bond line geometry, adherent geometry, and various connection methods on model response. Two exemplar geometries were explored: a double cantilever beam test and a single lap shear test. The results of this study were used to present guidelines and recommended practices for applying CZM to adhesive bond lines for a range of possible modelling scenarios. In the following, will be present the outcomes regarding the approach utilized in the work thesis:

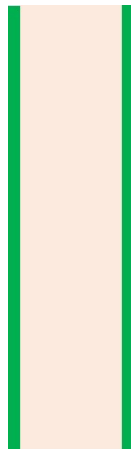


*Figure 3.3: Cohesive element between carbon fiber shell plies*

When modelling the adherent, with shell and the cohesive elements coincident with the midplane of the shell one, in fig 3.3, type 20 cohesive formulation is recommended. These cohesive elements may be connected to the shell elements of the adherent using either shared nodes or tied contact. However, this study has shown that type 20 cohesive elements may underpredict stiffness when placed under Mode II loading.

### 3.5 Crashworthiness test

As already mentioned before, usage of carbon fiber promotes the development of vehicles that meet safety standards with lower mass and noxious gas emissions. The high energy absorbing capacity is due to crashworthiness of the material. In order to have a correct prediction a specific test is necessary, in [7], article discusses the use of fiber-reinforced plastics in constructing primary crash structures for automobiles and presents a methodology for using crashworthiness results from in-plane impact tests on carbon fiber reinforced epoxy flat plates to tune material cards in Radioss using global and adaptive response search methods. The resulting virtual material model was validated by comparing the crashing behavior with results obtained from experiments conducted on a Formula SAE crash box.

et al. [8], a newly developed anti-buckling fixture to assess the in-plane crashworthiness of flat composite specimens. The fixture was designed by a team of researchers from Politecnico di Torino, Centro Ricerche Fiat, and Instron CEAST. The fixture overcomes the limitations of previously published solutions and includes cylindrical anti-buckling columns with adjustable heights. It is designed for rectangular specimens with dimensions of  $150 \times 100$  mm and different thicknesses up to 16 mm. The fixture allows for the study of the effects of different defects on the crashworthiness of composites, has a higher crashing area, and can be integrated with Instron drop tower and hydraulic testing machines. The article provides detailed information on the design process, materials, and methods used in the development of the fixture

### **3.6 State-of-the-Art consideration**

An in-depth overview of the state of the art in car safety crash systems, is presented, specifically the use of origami shapes and carbon fiber composites in energy-absorbing components, showing potentialities for these materials and techniques to improve the safety and performance of vehicles in motorsports and aerospace engineering. The various approaches to numerical modelling and testing demonstrate the complexity and rigour involved in designing and verifying these systems. The origami shape is a promising way to improve the dynamic crash behaviour of the carbon fiber in the passive safety system field. The geometry can guarantee a fracture-triggering effect in the crash box, which ensured a smaller peak force. The optimized origami crash box presents enhanced properties with respect to a conventional squared section crash box, in terms of crash efficiency. This confirmed the possibility to tune the crash and impact properties of a crash box by modifying its geometry without affecting its mass.

# Chapter 4

## Material Characterization

In this chapter will be presented the characterization phase of the utilized material, discussing the procedure and the methodologies.

The first section is regarding the prepreg carbon fiber cloth, highlighting the matrix and fiber properties. The next section is dedicated to a detailed description of the laboratory investigation tests to extract the material mechanical properties.

The last one will be related to the FEM material card parameter needed to run the model. Finally, a brief overview about failure theory.

### 4.1 Carbon Fiber Material: T300

The carbon fiber used, from this point on, will be the T300, a high-performance carbon fiber manufactured by Toray Industries. It is one of the most widely used carbon fiber grades in various industries due to its excellent mechanical properties and reliability. In the specific case, we will use a woven fabric **2×2 twill; 3k; 200gsm**, indicating respectively the wave patten of the fabrics; number of individual filament within a single tow or bundle of the carbon; and the density expressed in grams per square meter. The twill drape is widely used for several reasons: the cloth is balanced and show in the 0°, 90°orientation, more or less the same characteristics<sup>1</sup>. The wave pattern guarantees

---

<sup>1</sup>the carbon fiber is a high anisotropy material; his mechanical properties are different along the applied force direction

a good *drapability* of a fabric, referring to its ability to easily adapt or fold over a surface or around a three-dimensional shape without creating tension or unwanted deformations.

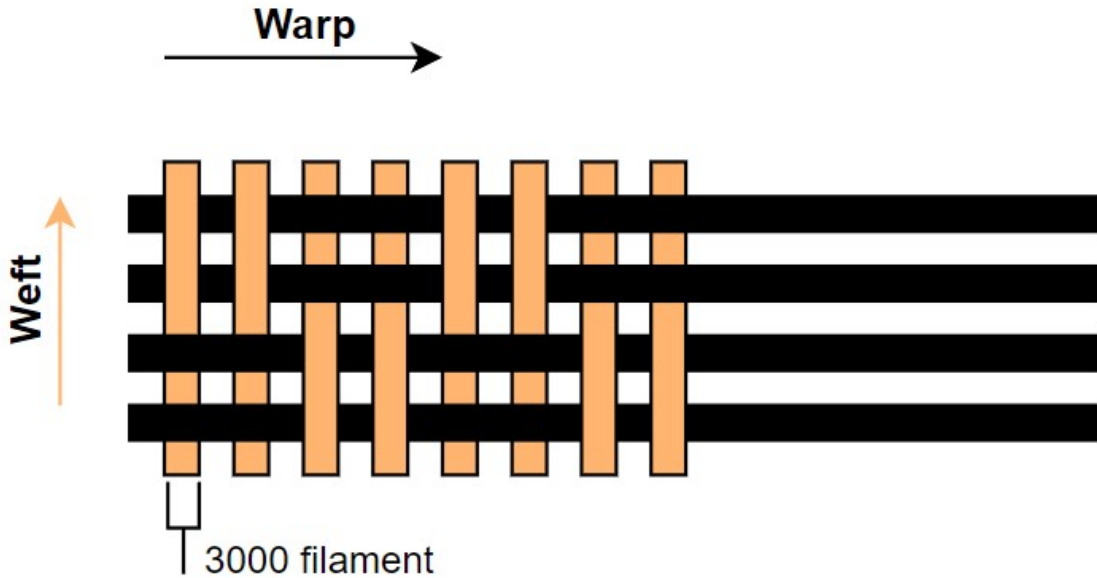


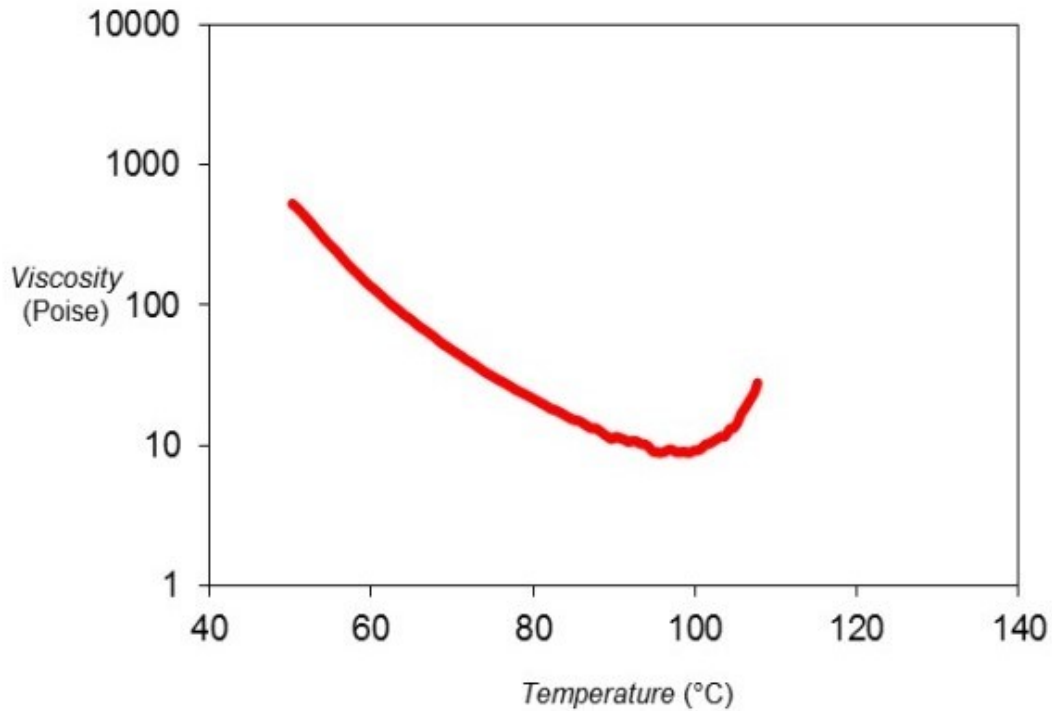
Figure 4.1: Woven Fabric 2x2 twill 3k

In figure 4.1 two principal direction are visible. The **warp** refers to the set of fibers running parallel to the length of the fabric, while the **weft** refers to the set of fibers running perpendicular to the warp.

## 4.2 Matrix Epoxy Resin: DT806W

T300 carbon fiber is compatible with a wide range of thermoset and thermoplastic resins. Its surface is often treated or sized to enhance adhesion with the matrix material, ensuring efficient load transfer between the fiber and the matrix. In our specific case, the epoxy resin is: DT806W-42, produced by DeltaPreg. It is suitable for processing by oven autoclave bag curing. The resin have a curing range temperature between 65-140°C, with the following viscosity profile 4.2.

In conclusion, the resultant material will be T300 combined with the resin DT806,



Source: <https://www.delta-preg.com/product-selector/>

Figure 4.2: DT806 Temperature Viscosity Profile

pre-impregnated by the reseller DeltaPreg; resulting in a uniform distribution of the resin among the carbon fibers. As mentioned in chapter 3, a correct impregnation is necessary to have a good load distribution along the fiber direction.

## 4.3 Tensile Test Characterization

ASTM D3039 [9] is the standard test followed to evaluate the mechanical properties of the specimens realized in T300 prepreg with DT806 epoxy resin. The norm is used to determine the tensile properties of fiber-reinforced polymer matrix composites.

### 4.3.1 Specimen production

The specimens have been derived by an autoclave cured plate.

For the production, a pre detached plate was placed on the base, where, the plies were

CHAPTER 4. MATERIAL CHARACTERIZATION

---

stacked; after lamination, on top, a second detached plate (of the same size as the plies to prevent bending under the pressure of the bag and autoclave) was positioned, and finally, everything was bagged. The production of the prepreg specimens was carried out using an autoclave cycle at approximately 5 bar and 135°C for 8 hours.

TENSILE SPECIMEN LAYUP		
PLY	PREPREG	DIRECTION
1	T300 200gsm T2x2	0/90°
2	T300 200gsm T2x2	0/90°
3	T300 200gsm T2x2	0/90°
4	T300 200gsm T2x2	0/90°
5	T300 200gsm T2x2	0/90°
6	T300 200gsm T2x2	0/90°
7	T300 200gsm T2x2	0/90°
8	T300 200gsm T2x2	0/90°
9	T300 200gsm T2x2	0/90°
10	T300 200gsm T2x2	0/90°
11	T300 200gsm T2x2	0/90°
12	T300 200gsm T2x2	0/90°
13	T300 200gsm T2x2	0/90°

Table 4.1: Tensile specimen layup

	Tensile Specimen Dimension			
	T1	T2	T3	T4
Thickness	2.85	2.83	2.85	2.9
Length	250	250	250	250
Width	25.19	25.15	25.18	25.27
Cut Direction	0°	0°	0°	90°

Table 4.2: Tensile specimen dimension

In the picture are notable strain gauges(HBM 1-LY48-3/350), utilized to read in the fracture zone the load and the strain applied to our specimen, that are summarized in table 4.2.



*Figure 4.3: Tensile Specimen-before the test*

On the specimens were being applied strain gauges to measure the load and strain effect on the failure zone. In the figure 4.3 they are visible.

### **4.3.2 Tensile Test Procedure**

The tensile procedure has been conducted with a servo hydraulics Instron 8801 machine. A preload force, of around 5kN, was applied to the specimens in order to consolidate each sample. When the preload was applied, the effective test started and the strain gauge (HBM 1-LY48-3/350) was active and stored the data during all the process. For the specimen T2, the strain gauge broke during the test; for the post process, it will not be considered. The breaks of the specimens can be considered acceptable according to the standard ASTM norm. The figure 4.4 shows the break points along the samples' length. For specimen T1, T2, and T3 the breakage is still acceptable because it is outside the grip zone; instead, for the last sample T4, a perfect fracture is visible on the mid-length point. A pressure of 200bar was applied to the gripping head in order to prevent

slippage.



Figure 4.4: Tensile Specimen – after the test

Apart from perfect fracture in specimen 4, the other three specimens are acceptable for ASTM standard because the fracture is out of the clamping zone machine.

## 4.4 Compression Test Characterization

The ASTM D3410 [10] is the followed standard for the characterization phase of the compression properties of the laminate T300-DT806W, indeed the norm have a restricted procedure to fulfil correctly the test. For our purpose, a compliant test bench, it has been utilized in order to prevent the bucking effect of the specimen in compression mode, figure 4.5

### 4.4.1 Specimen production

The specimen has been derived by an autoclave cured plate with the same curing cycle as the tensile plate. The ASTM standard was also followed to determine the thickness of the specimen, with the following equation:

$$h \geq \frac{l_g}{0.9069 * \sqrt{\left(1 - \frac{1.2F_{cu}}{G_{xz}}\right) \left(\frac{E^c}{F_{cu}}\right)}} \quad (4.1)$$

Putting all material data;  $h$  will be 3 mm of thickness. In the following, the layup process for compressive plate

COMPRESSION SPECIMEN LAYUP		
PLY	PREPREG	DIRECTION
1	T300 200gsm T2x2	0/90°
2	T300 200gsm T2x2	0/90°
3	T300 200gsm T2x2	0/90°
4	T300 200gsm T2x2	0/90°
5	T300 200gsm T2x2	0/90°
6	T300 200gsm T2x2	0/90°
7	T300 200gsm T2x2	0/90°
8	T300 200gsm T2x2	0/90°
9	T300 200gsm T2x2	0/90°
10	T300 200gsm T2x2	0/90°
11	T300 200gsm T2x2	0/90°
12	T300 200gsm T2x2	0/90°
13	T300 200gsm T2x2	0/90°

Table 4.3: Tensile specimen layup

The prepreg ply post cured is roughly 0.23 mm of thickness; calculated from the total plate thickness dividing for #layup plies. In table 4.4 summarized the geometry dimension of each sample utilized during characterization campaign.

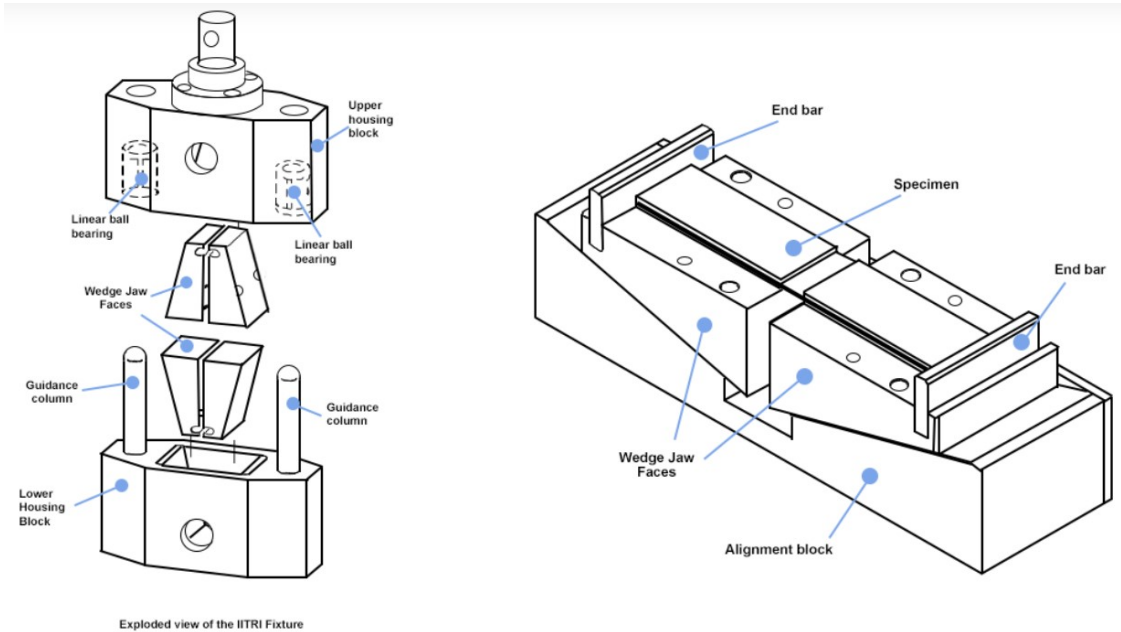
Compression Specimens Dimension						
	T1	T2	T3	T4	T5	T6
Thickness	2.91	3.04	3.03	2.99	2.97	2.98
Length	155	155	155	155	155	155
Width	25.04	24.95	25.02	25.03	24.95	25.03
Cut Direction	0°	0°	0°	0°	0°	90°

Table 4.4: Compression specimen dimension

In table 4.4 all the geometrical specimen dimension are summarized.

### 4.4.2 Compression Test Procedure

As already mentioned in the previous section, a specific test fixture is being used in order to avoid the buckling effect of the specimen, figure 4.5. A preload force of around 5kN has been applied to each specimen to correct settle it and the fixture.



Source: <https://www.instron.com/en/testing-solutions/astm-standards/astm-d3410>

Figure 4.5: Test fixture for compression characterization

For compression test, the buckling effect<sup>2</sup> is crucial. The standard propose to correct place the specimen, an inclined block, maintaining the sample as straight as possible and parallel to the reference plane.

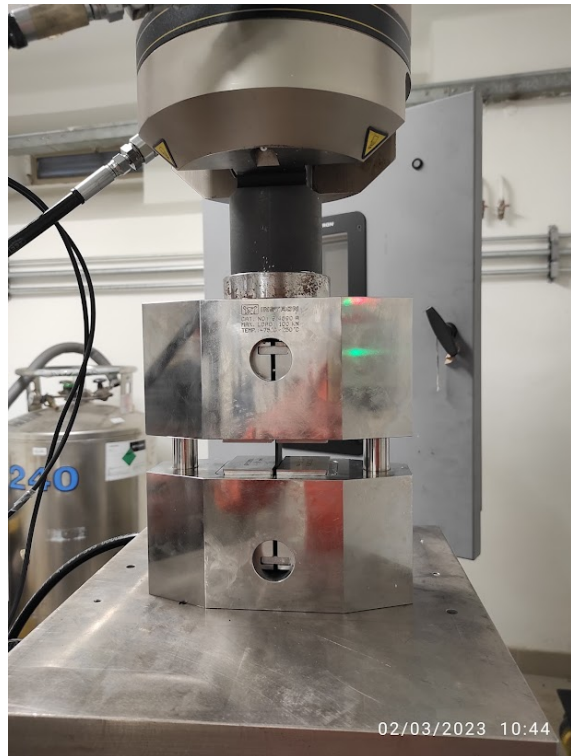
The specimen had shown a correct breakage, acceptable from the standard point of view, in fact, the failure happens in the free area of the specimen. In addition, a clear barrel breaking is visible in last figure 4.6d. For compressive test, HBM 1-LY48-3/350

<sup>2</sup>structural instability that can occur in slender columns, subjected to compressive loads. The member deviates from its straight, stable configuration and undergoes large deflections or deformations, inducing shear and combined stresses.

strain gauges were used. To capture the signal and convert the resistance strain gauges variation, LabView acquisition board was used. Before the test, an already implemented Wiston bridge was utilized to calibrate the strain sensor.



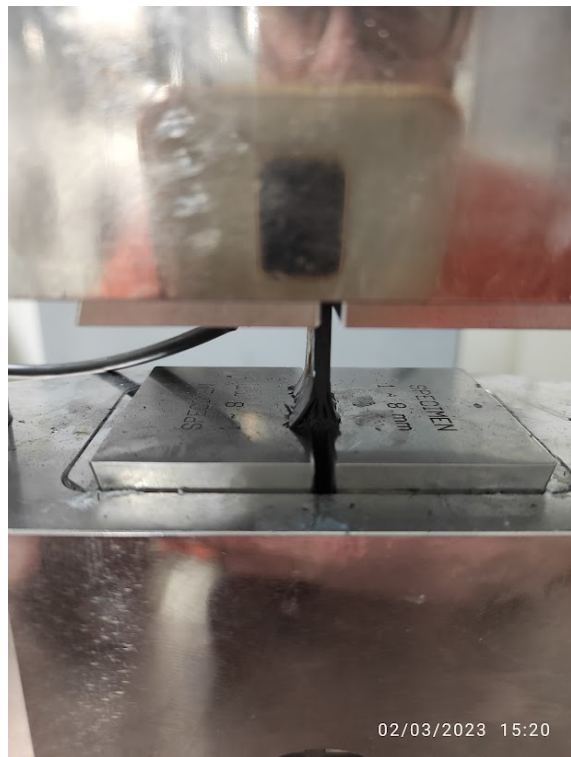
(a) Specimen with strain gauges applied



(b) T2 specimen placed in test fixture



(c) Compression specimen-after the test



(d) Detailed specimen breakage

## 4.5 Material post process data

In the following section, data post process will be discussed; highlighting the mechanical characteristics extracted from the experimental test.

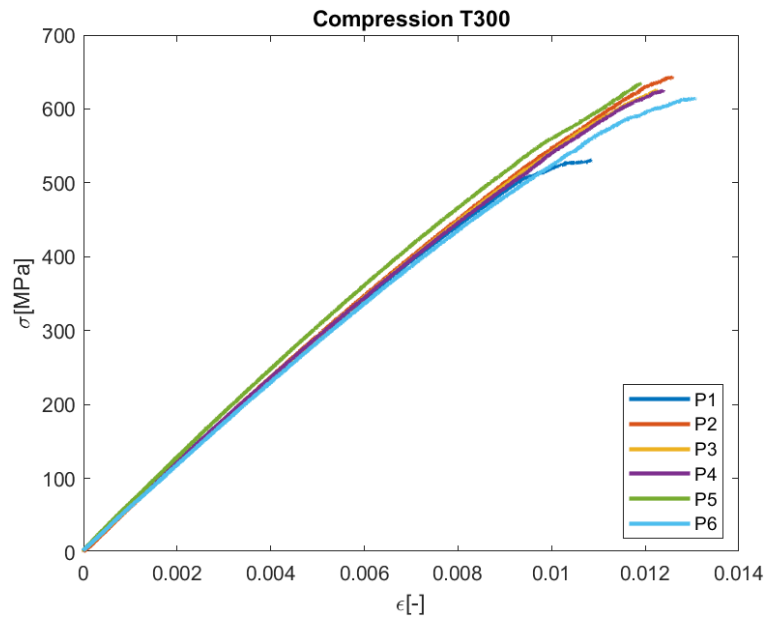
### **From tensile characterization tests:**

- UTS: Ultimate Tensile Strength
- Tensile modulus of elasticity

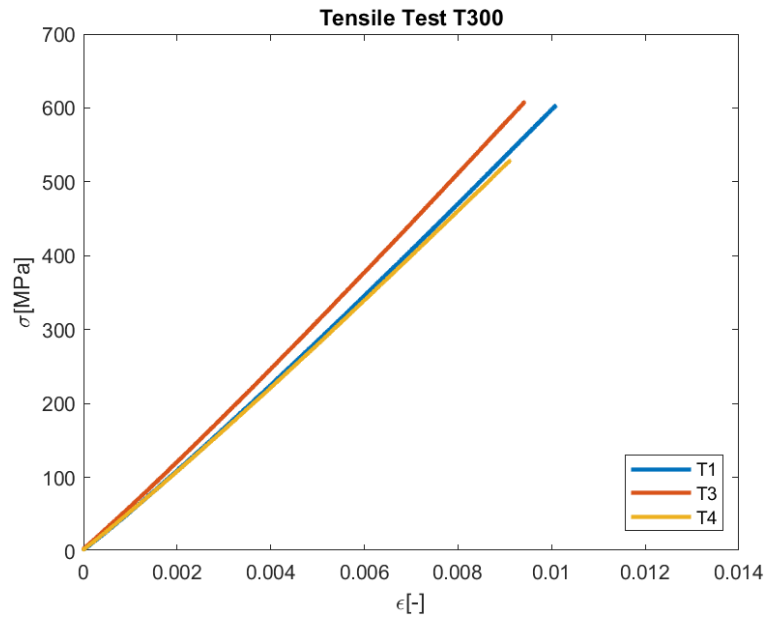
### **From compression characterization tests:**

- UCS: Ultimate Compressive Strength
- Compressive modulus of elasticity

CFRP shown a brittle material, so no ductile behaviour will be visible in the  $\sigma - \epsilon$  (stress-strain) curve. The curing autoclave cycle had permit to have a good repeatability of the test, in fact, the curves are roughly overlapping each other. A slight difference is visible for the cutted specimen in 90° direction: although the carbon fiber tissue was a twill 2×2 in the production phase can have a small changing between warp and weft number of fiber.



(a) Stress-strain **compression** characteristic



(b) Stress-strain **tensile** characteristic

Figure 4.7: Mechanical tensile/compression curve

The **Ultimate Tensile Strength** and **Ultimate Compression Strength** will be calculated with an average between the sample. For what concern the Young modulus

was evaluated in the region 45 MPa-200 MPa where the curves show a good linear behaviour. All the mechanical quantities are summarized in table 4.5

	<b>UTS [MPa]</b>	<b>E_T [GPa]</b>
<b>Tensile</b> , ASTM D3039	605	57.90
	<b>UCS [MPa]</b>	<b>E_C [GPa]</b>
<b>Compression</b> , ASTM D3410	611	57.94

Table 4.5: Material Properties

## 4.6 Material Card

Material Cards are used to define the material properties of different elements and is an essential component of the input deck of FEM software. These allow specifying the behavior and characteristics of materials used in simulation. typically includes the following information:

- **Material type:** specifies the mechanical behaviour
- **Material parameters and properties:** physical and not one, for loading condition
- **Failure criteria:** regarding the element deletion

Mentioned in 3 the utilized material card:

- MAT 054-055: MAT ENHANCED COMPOSITE DAMAGE
- MAT 138: MAT COHESIVE MIXED MODE

### 4.6.1 MAT 054

Material Types 54-55 in LS-DYNA refer to the MAT ENHANCED COMPOSITE DAMAGE material model. It is an orthotropic material model that can be used to define orthotropic

materials, such as in composite shell structures. MAT 54 follows **Chang Matrix Failure Criterion**. The key point of the following equation is the failure flag. The failure flag  $e$  indicates the state element. If the failure flag is major or equal to zero ( $e \geq 0$ ) the element is failed, otherwise is elastic. The failures flag can be referred to the fibers and matrix in order to separate the contribution between matrix and fibers. In addition, it is possible to express them in tensile and compression load case.

- Tensile Fiber State

$$e_f^2 = \left( \frac{\sigma_{aa}}{X_t} \right) + \beta \left( \frac{\sigma_{ab}}{S_c} \right) \quad (4.2)$$

- Compression Fiber State

$$e_c^2 = \left( \frac{\sigma_{aa}}{X_c} \right) - 1 \quad (4.3)$$

- Tensile Matrix State

$$e_m^2 = \left( \frac{\sigma_{bb}}{Y_t} \right) + \left( \frac{\sigma_{ab}}{S_c} \right) - 1 \quad (4.4)$$

- Compression Matrix State

$$e_d^2 = \left( \frac{\sigma_{bb}}{2S_c} \right) + \left[ \left( \frac{Y_c}{2S_c} \right)^2 - 1 \right] \frac{\sigma_{bb}}{Y_c} + \left( \frac{\sigma_{ab}}{S_c} \right)^2 - 1 \quad (4.5)$$

Where:

$aa =$  Fiber direction

$bb =$  Matrix direction

$Xc =$  Longitudinal Compressive Strenght

$Xt =$  Longitudinal Tensile Strenght

$Yc =$  Transverse Compressive Strenght

$Yt =$  Transverse Tensile Strenght

$Sc =$  Shear Streght.

The above equation governs the failure flags. We think about them like a safety factor in the mechanical domain, in fact, we evaluate the ratio between the effective stress

along the interested direction over the stress limit. If the load stress overcome the permissible stress, failure occurs.

### 4.6.2 MAT 54 PARAMETER

To conclude the section related to Material 54, a list of the parameters needed to correctly describe the phenomenon. In the following table will be listed all the used parameter, creating also a link with characterization data found in the previous subsection.

<b>MID</b>	<b>RO</b>	<b>EA</b>	<b>EB</b>	<b>(EC)</b>	<b>PRBA</b>		
1	1.472e-06	58	58	0.0	0.083		
<b>GAB</b>	<b>GBC</b>	<b>GCA</b>	<b>(KF)</b>	<b>AOPT</b>	<b>2WAY</b>	<b>TI</b>	
4	4	4	0.0	-1	1	0.0	
			<b>A1</b>	<b>A2</b>	<b>A3</b>	<b>MANGLE</b>	
			0.0	0.0	0.0	1	
			<b>D1</b>	<b>D2</b>	<b>D3</b>	<b>DFAILM</b>	<b>DFAILS</b>
			0.0	1	0.0	0.02	0.0411442
<b>TFAIL</b>	<b>ALPH</b>	<b>SOFT</b>	<b>FBRT</b>	<b>YCFAC</b>	<b>DFAILT</b>	<b>DFAILC</b>	<b>EFS</b>
1.100e-06	0.0	0.65	0.0	2	0.3453858	-0.1	0.0
<b>XC</b>	<b>XT</b>	<b>YC</b>	<b>YT</b>	<b>SC</b>	<b>CRIT</b>	<b>BETA</b>	
-0.612	0.605	-0.612	0.605	0.065	54.0	0.32	
<b>SLIMT1</b>	<b>SLIMC1</b>	<b>SLIMT2</b>	<b>SLIMC2</b>	<b>SLIMS</b>	<b>NCYRED</b>	<b>SOFTG</b>	
0.01	1	0.1	1	1	0.0	0.0	

Table 4.6: MAT 54 input data

In LS-Dyna the units of measurement are not introduced. The idea is to be coherent, and put in a correct way all the data without a precise label. In this case, data in table 4.6 follow these units of measurement:

$$Mass = kg$$

$$Lenght = mm$$

$$Time = ms$$

Taking into account this assumption, the forces, and the stresses will be expressed with  $Force = [kN]$ ,  $Stress = [GPa]$

Not all the parameters were determined from scratch; for several of them, the starting points were the experimental parameters found in the [7]. From these parameters, the process to correctly balance the material card, due to the material similarity.

In addition, the **SLIMx** parameters were setted in accordance to [11] in order to do not have instabilities during simulation.

### 4.6.3 MAT 138

Material Type 138, follows a traction-separation law with a delamination criterion. This material model is compatible only with cohesive element formulations. It was used in the thesis work in order to capture the delamination effect during a crash event. In particular, this approach, helps in the thick specimen zone, where failure modes are appreciable.

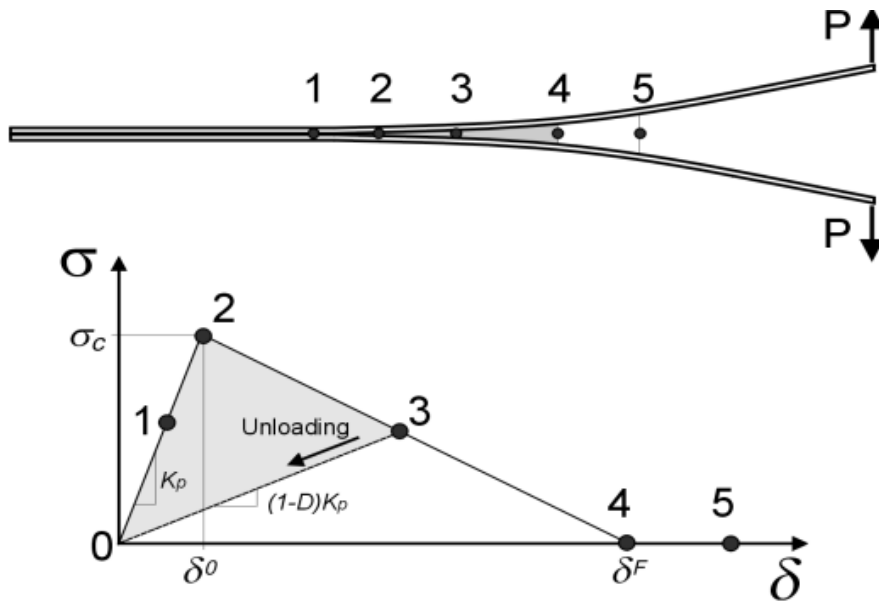


Figure 4.8: MAT 138 – Constitutive model [12]

In the segment 0 – 1, the material shows elastic deformation. Proceeding with load, from the point 2 the damage starts in fact, continuing toward point 3 the stress is decreasing. From now, the delamination process between plies starting and the  $\delta$  offset between plies increase.  $Area_{024}$  represent the fracture energy.

That behaviour is valid in normal direction; law must be extended in mixed mode, taking into account, at the same time, *MODE I* & *MODE II*

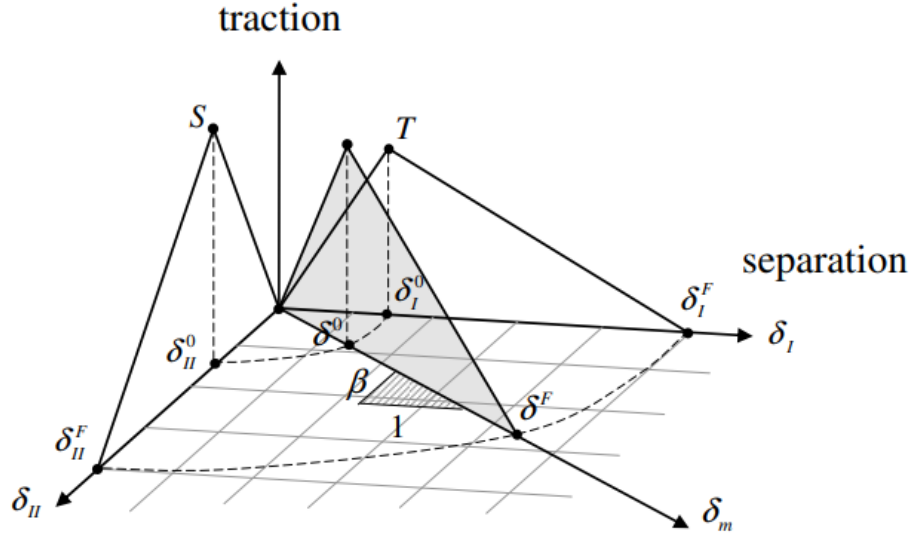


Figure 4.9: MAT 138 – Mixed Mode

The relative displacement between plies is shorted in just one, as follows:

$$\delta_m = \sqrt{\delta_I^2 + \delta_{II}^2} \quad (4.6)$$

$$\delta_{II} = \sqrt{\delta_1^2 + \delta_2^2} \quad (4.7)$$

Due to the fact that **MODE I** is regarding the normal displacement:

$$\delta_I = \delta_3 \quad (4.8)$$

where:

$\delta_1; \delta_2; \delta_3$  : displacement between plies

$\delta_I; \delta_{II}; \delta_{III}$  : tangent displacement

The delamination effect is described through a power law equation; the equation terms represent triangles area in 4.9.

$$\left(\frac{G_I}{G_{IC}}\right)^\alpha + \left(\frac{G_{II}}{G_{IIC}}\right)^\alpha = 1 \quad (4.9)$$

In the same failure flag way, presented in previous section, the delamination is described by ratio between energy state over critical energy; separated in two contribution: normal *I* and shear direction *II*.

#### 4.6.4 MAT 138 PARAMETER

The input parameter in material card 138 are referring to work done by [8], in which experimental characterization test were conduct to investigate the cohesive parameter. Starting from that, based on experimental curve in the next chapter, a calibration process has been implemented in order to fit correctly the delamination effect. In the table 4.7 the input deck:

<b>MID</b>	<b>RO</b>	<b>ROFLG</b>	<b>INTFAIL</b>	<b>EN</b>	<b>ET</b>	<b>GIC</b>	<b>GIIC</b>
2	1.000e-07	0.0	1.0000000	1.1670001	4.1599998	0.0054480	0.0011774
<b>XMU</b>	<b>I</b>	<b>S</b>	<b>UND</b>	<b>UTD</b>	<b>GAMMA</b>		
1.0000000	0.0800000	0.0700000	0.0686000	0.0168200	1.0000000		

*Table 4.7: MAT 138 input data*

# Chapter 5

## Impact Attenuator Design and Production

The chapter will be articulated as follows: in the first section a brief introduction about origami shape and its parameter. The following one will regard the design choices, concluding with mould and specimen production.

### 5.1 Origami Shape

The term *Origami*, refers to the art of folding, in general paper, into various shapes and forms. For crash investigation purpose, the paper is substituted by CFRP. The objective of using the origami technique is to realize a crash box having a squared frontal area. Et al. [13], geometrical functions were found to correctly describe the origami shape.

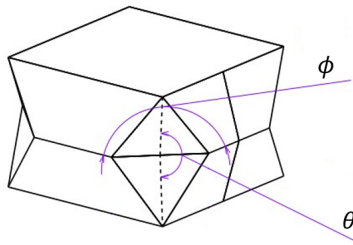


Figure 5.1: Characteristic origami crash box angles [13]

The global function describing correlation between  $\phi$  and  $\theta$  angles is the following:

$$\phi = \pi - 4 \arctan \left( \frac{l}{c} \cos \frac{\theta}{2} \right) \quad (5.1)$$

In order to have a squared crash box,  $\phi = \frac{\pi}{2}$ ; so the main relation become 5.2.

$$\cos \frac{\theta}{2} = (\sqrt{2} - 1) \frac{c}{l} \quad (5.2)$$

Authors, et al.[14] describe the elementary origami structure module. The single module can be stacked to create a complete crash box. In figure 5.2 a single module is presented in **folded** and **unfolded** configuration.

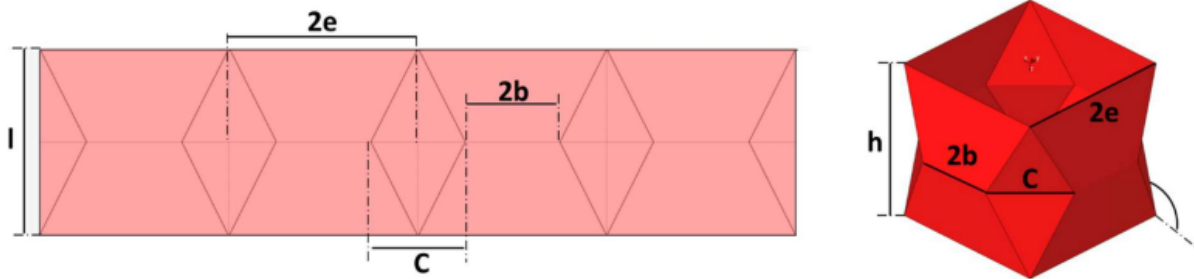


Figure 5.2: Single origami structure model [14]

The origami tube is characterized in its folded configuration by two cross-section: squared and octagonal.

In order to have a perfect rectangular unfolded plies, a boundary condition must be true.

$$Perimeter_{squared\ section} = Perimeter_{octagonal\ section} \quad (5.3)$$

To fulfil the requirement, the following relation will be valid; so substituting the perimeter elements, what we have is:

$$8e = 8b + 4c \quad (5.4)$$

where

$c =$  width of rhomoidal lobe

$h =$  distance between the two squared section

$h \neq l$  because a  $\theta$  angle born during folding process

## 5.2 Geometry Design

In the previous section, the main geometrical parameter of the origami crash-box geometry are presented. Now will be discussed the geometrical design choices before starting the presentation of the production phase of the tested specimen.

### 5.2.1 Geometry

The Impact Attenuator structure has some geometrical needs that must be satisfied, in order to be accepted by FSAE rules and procedure. To save weight and material in production phase, minimum dimensions, already presented in chapter 2, for the crash box absorber, were chosen. The dimension of a single crash box will be:

$$100 \times 100 \times 210 \text{ mm}^3$$

each, composed by three modules with dimension

$$100 \times 100 \times 70 \text{ mm}^3$$

In addition, to facilitate the production, saving money, the final configuration is characterized by two crash boxes in parallel mode. This is because a single mould will be needed to produce the IA structure, saving material during machining. In figure 5.3 the main characteristic angle and dimension of a single module are presented.

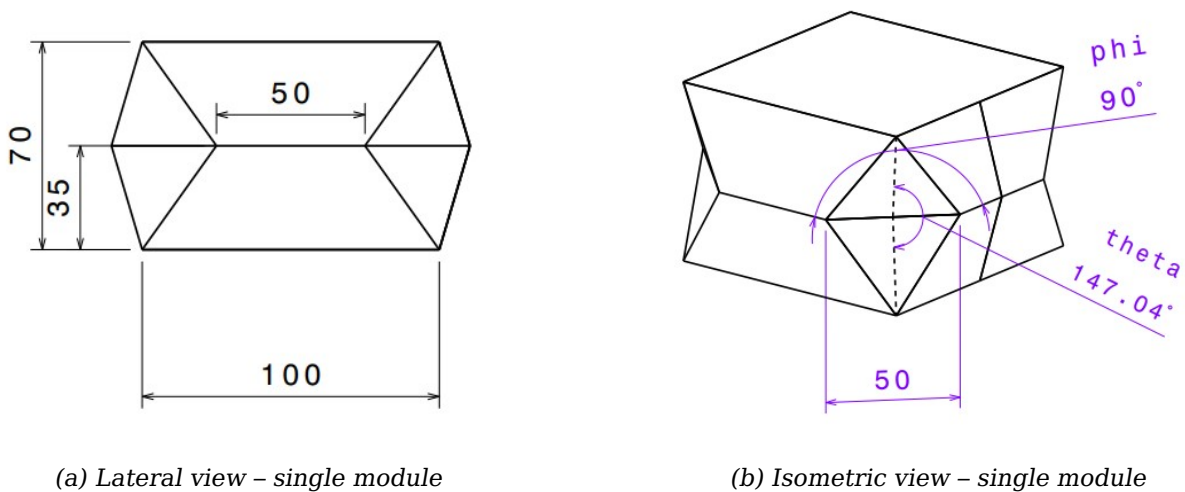


Figure 5.3: Single module dimension

The final crash box is a sequence of three laminated modules. To realize a carbon fiber part, a mould is necessary; in consequence of that, a clearance angle is necessary, and it will be mandatory to correct extract the piece after curing process. In following figure 5.4 the final dimension of the crash box.

In the frontal view, it is appreciable the clearance angle of  $3.1^\circ$  needed for de-moulding operation.

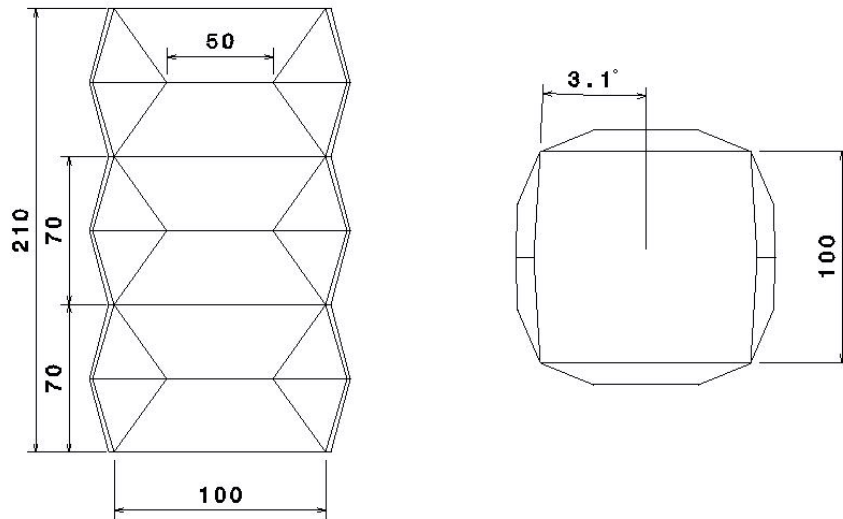


Figure 5.4: Single crash box dimension

## 5.3 IA Specimen Production

For component production using carbon fiber a mould is needed; a solid surface where each CFRP plies will be laminated. In particular case, we can have also disposable mould. In ours, what we have produced is a female mould. Using the following two material:

- Female mould – Epoxy resin WB 700
- Female mould – Aluminium series 3000

### 5.3.1 WB 700 epoxy mould

The first approach was to use only an epoxy mould. The main drawbacks related to this, is the several specimen lamination, in fact, the resin mould suffers with every

lamination and curing process. In addition, a poor surface quality is achieved by the resin with respect to Al due to the nature of the material and its density of  $700 \frac{kg}{m^3}$ . The crash box geometry presents a lot of undercut due to inclined faces for rhomboidal cross-section junction. One division plane is the minimum number to have the possibility to extract the crash box without problems. Apart from the technical point of view, also in terms of manufacturing the split of the geometry in two component was useful.

The starting point to create the mould was the crash box CAD model presented in figure 5.4. For the first epoxy mould, an  $1^\circ$  of extraction angle was used; resulting in a difficult demoulding operation; instead, for Al mould  $3^\circ$  was chosen to facilitate the manoeuvre and not risk damaging the crash box. The extraction plane, it has been placed in the middle of the transversal dimension of the crash box.

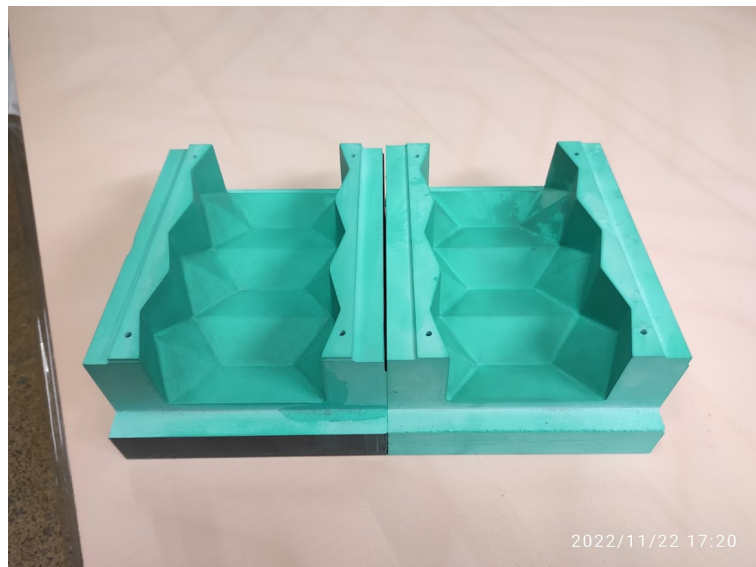


*Figure 5.5: Epoxy resin mould – WB 700*

In the figure 5.5 the two mould surface are visible. A wall thickness of  $20mm$  it was expected in order to prevent damage during expansion of the carbon fiber piece. The two mould parts are complementary; after the lamination will be reversed, one on top of the other. Four centering holes are present, to avoid misalignments.

For epoxy mould, before lamination process a pre-treatment is needed. The operation have been:

- Sandpaper P400
- Sandpaper P600
- Sandpaper P1000

- Pore filler (5 times; 1d air drying)
- Agent release (5 times; 1h air drying)

The sandpaper was chosen to have a better quality surface of the component. Instead, the pore filler is used with epoxy mould to fill micro imperfection of the surface. Finally, an agent release is needed to facilitate the release between mould and final piece after curing process. Now mould is ready for lamination process.

The sharp geometrical edges in the mould are not present because the cutting tool has a  $3mm$  radius. This is useful also for the layup process, not preventing the sharp changing in the fiber direction. So the final piece will have  $3mm$  of fillet radius.

### 5.3.2 Al mould

The manual operation required for Al mould are less with respect to the previous one. Only the agent release is still needed to prevent bonding between mould and component. The quality surface for Al material is good enough after machining, so no other sandpaper operation are required. Duration over time for Al mould is the key aspect.

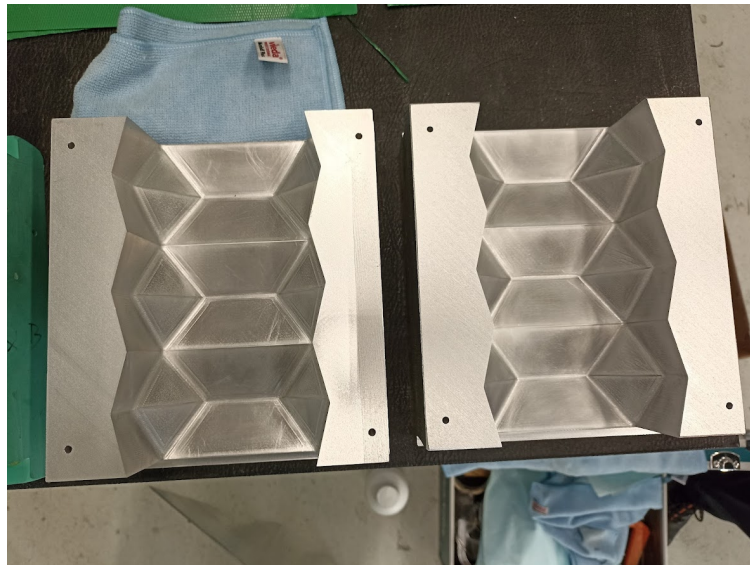


*Figure 5.6: Aluminium mould*

As said for the epoxy mould, also in this case  $3mm$  fillet radius, it has been used.

### 5.3.3 Hand Layup Specimen Lamination

To validate the numerical model, and have a good statistical sample; seven (7) specimens have been laminated and crashed. To have a progressive energy absorption and a not sudden deceleration, each module have different plies.

For validation specimen, the layup was: 3-6-9 T300 plies. As follows:

Module1: 3 plies (dim: 200×218mm)

Module2: 6 plies (dim: 200×148mm)

Module3: 9 plies (dim: 200×80mm)

The final laminate thickness is respectively: 0.69-1.38-2.07 (mm) considering 0.23mm each plies. In order to have no sharp plies changes between one module to the following one, a particular reasoning was used. In the following, a picture will figure out the idea to better explain.



*Figure 5.7:*  
3 modules plies



*Figure 5.8:*  
2 modules plies



*Figure 5.9:*  
1 modules plies

Starting from the left side, picture 5.7, the three modules plies will be able to cover all crash box modules. In the same way, the two modules plies, will cover only two of them and so on for the last plies.

This idea was used to have a progressive increasing in plies thickness without cutting as less as possible the CFRP. This will increase in the crash box performance due to continuity of the carbon fibers and an easier lamination process.

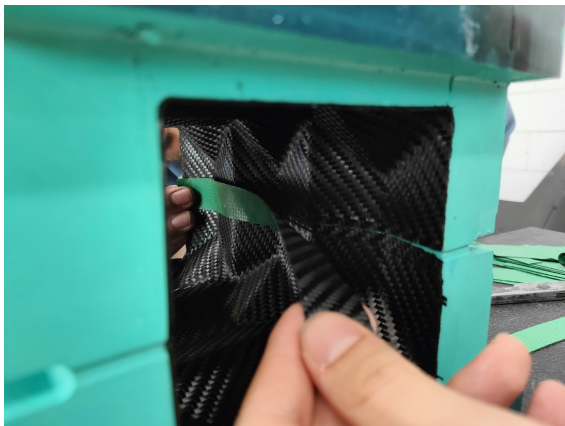
The main problem was to connect the two crash box half reducing defect in the zone of extraction plane.

Two method have been studied:

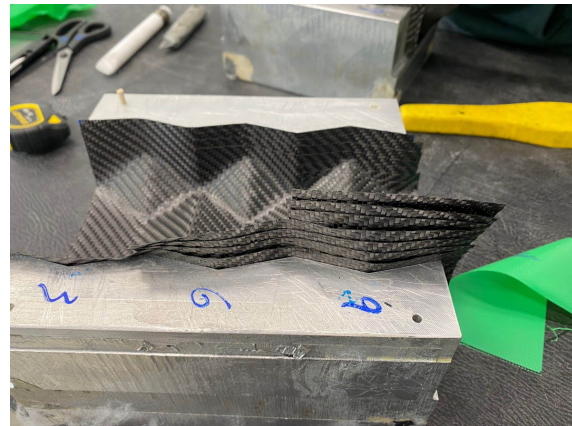
- **Strip method**

- **Overlapping method**

For the *Strip method*, the two half crash box part are laminated separately, only when the mould is positioned on top of the other some strips (20mm of width) are added to bonding the upper and lower member part of the box. In the figure 5.10a the added strips are visible.



(a) Strip connection two crash box half



(b) Overlap production plies

Figure 5.10: Production methods: Strip and Overlap

After curing process, strip specimens present in the junction zone, a variation in thickness, translated in a defect during impact event.

For the second production method, called **overlap**, the plies are positioned in complementary way in the two moulds. To better visualize the situation, in addition to figure 5.10b a clear scheme is attached 5.11:

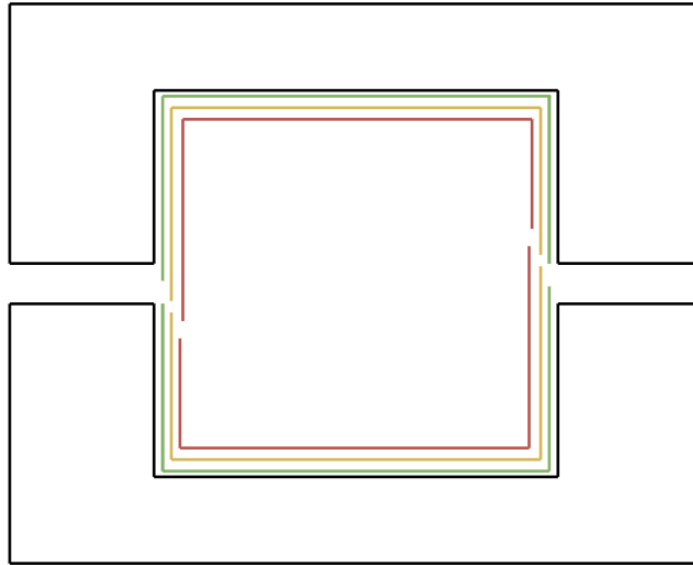


Figure 5.11: Overlap criteria

The plies are scaled of 5mm. The main difference with respect to the strip method is a better junction between the two shell. In the next chapter will be discussed, in detail, the effect during crash event.

Now the lamination order is summarized in the table. Organized in the plies order, typologies, and intermediate operations.

PLY	PREPREG	DIRECTION	Increment module 1	Increment module2	Increment module 3
3	T300 200gsm T2x2	0/90°	1	1	1
	PRE-VACUUM				
3	T300 200gsm T2x2	0/90°	1	1	1
2	T300 200gsm T2x2	0/90°	-	1	1
2	T300 200gsm T2x2	0/90°	-	1	1
2	T300 200gsm T2x2	0/90°	-	1	1
1	T300 200gsm T2x2	0/90°	-	-	1
1	T300 200gsm T2x2	0/90°	-	-	1
1	T300 200gsm T2x2	0/90°	-	-	1
3	T300 200gsm T2x2	0/90°	1	1	1
<b>Total plies</b>			<b>3</b>	<b>6</b>	<b>9</b>

Table 5.1: Layup validation specimens

### 5.3.4 Specimen notation

To better understand the correct nomenclature of the specimen, the following code will be used:

**batch - test type - specimen number - production type**

where the batch and the test type are the same for all.

batch: **10262**  
test type: **crash(C)**  
production method: **Strip (S); Overlap (O)**

As an example, the first specimen code is:

**10262\_C\_1(S)**

The lamination order for validation specimen was the same for all; the change is in the production method. A total of seven specimens were produced to validate the numerical model presented in the next chapter.

10262\_C\_1;10262\_C\_2;10262\_C\_3;10262\_C\_5;10262\_C\_6: **Strip specimen**  
10262\_C\_4;10262\_C\_7: **Overlap specimen**

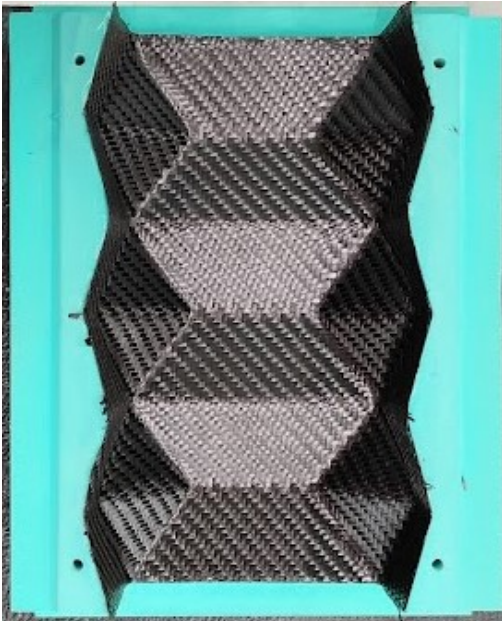


*Figure 5.12: Impact validation specimen*

In figure 5.12 two Impact specimen are depicted. The left side specimen was born by Al mould lamination; instead, the right one from the epoxy mould. The surface's imperfection are clearly visible: in the sharp edges of the origami structure, some epoxy residual remains attached to the specimen. The autoclave curing cycle of the specimen will be  $6bar$  at  $135^\circ$  for 3h, using vacuum bag.

A film release was used in order to prevent that the carbon fiber during the cure, remains attached to the breather. A  $300\frac{g}{m^2}$  breather was also applied in order to correctly distribute the pressure along the specimen; this one was added all around. For vacuum bag it was not utilized a self-releasing tubular bagging film because the opening faces of the crash box permits the normal vacuum bag, with dimension of  $1500\times 1500mm$ , to go into the mould and press uniformly.

To conclude, some production photos are attached 5.13



(a) Lamination process



(b) Film release



(c) Breather



(d) Pre vacuum bagging

Figure 5.13: Production photos

# Chapter 6

## Experimental Test

In this chapter we discuss the test procedure and the data processing to validate the numerical model. The tests were conducted thanks to the Centro Sicurezza Stellantis Group that helps to realize the experimental test and treat the out coming data. Before starting with data and test procedure a clear introduction about conditions, instrumentation, and acquisition sensor is faced. Proceeding with the treatment through the post process of the data from the sensor and from the recorded video, to finally conclude with some final consideration.

### 6.1 Test Rig

To test the seven specimen a *sled hammer* was used. The potential energy is converted during the falling in kinetic one. In figure 6.1 a schematic representation is depicted.

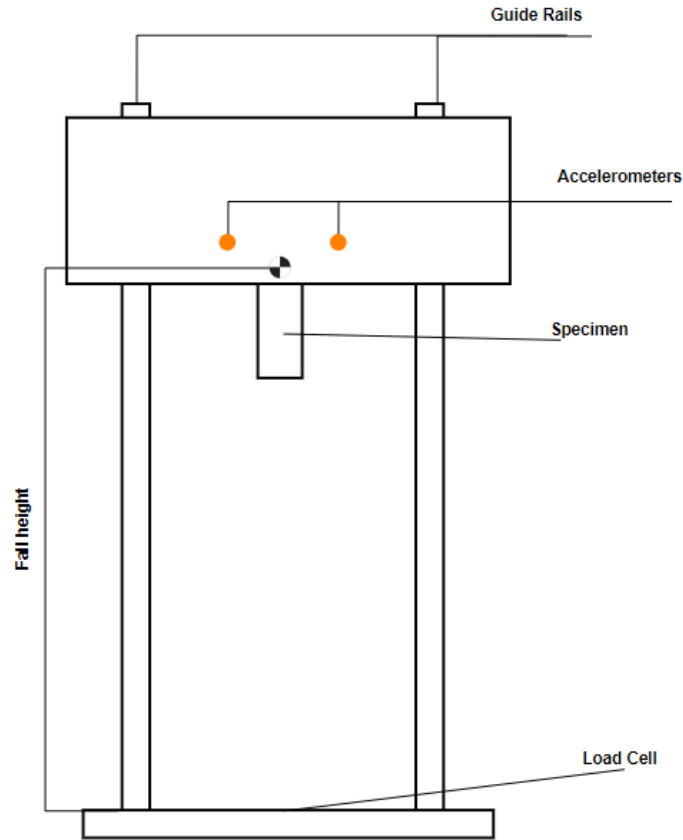


Figure 6.1: sled hammer scheme

The specimen is attached to the moving hammer head, this one with a mass of 480kg. Provided energy is dictated by fall height, this one calculated from the centre of gravity of the system.

$$E_k = E_p \quad (6.1)$$

$$mgh = \frac{1}{2}mv^2 \quad (6.2)$$

Three sensor are present on the sled hammer. From the top, two mono-axial accelerometer are positioned left and right to the specimen. To capture the force signal a load cell, at the bottom of the structure. All the three sensor are coordinated by a trigger presents on the load cell. When the specimen impacts on the load cell surface, trigger sends the acquisition command to the intended board. Finally, the camera also starts registration on trigger time.

## 6.2 Specimen Data

In table 6.1, specimen weight and energy provided for each test is presented. The main idea was to investigate the maximum energy absorption, meaning no residual material after the test. Excluding the specimen 1, form 2, an incremental energy was provided. In order to have comparable data the specimen 4 5 6 and 7 have been tested with the same amount of energy (3200J). The fall height was measured tacking measure of distance between load cell and centre of gravity.

SPECIMEN	CODE	WEIGHT [g]	FALL HEIGHT [m]	ENERGY [J]
1	10262_C_01_(S)	168	1.77	8334
2	10262_C_02_(S)	174	0.53	2496
3	10262_C_03_(S)	174	0.55	2590
<b>4</b>	<b>10262_C_04_(O)</b>	174	0.68	<b>3200</b>
<b>5</b>	<b>10262_C_05_(S)</b>	176	0.68	<b>3200</b>
<b>6</b>	<b>10262_C_06_(S)</b>	173	0.68	<b>3200</b>
<b>7</b>	<b>10262_C_07_(O)</b>	176	0.68	<b>3200</b>

Table 6.1: Specimen Test Condition

## 6.3 Acquired data

the acquired data are:

- acceleration signal: left accelerometer
- acceleration signal: right accelerometer
- force signal: load cell

All the sensor were synchronized by a trigger positioned on the load cell, meaning that the array acceleration and force size were the same.

With a frequency sample acquisition of 20kHz, resulting in a  $dt = \frac{1}{20000} = 5e - 5s$ , the signals were being sampled. An analogic filter of 5000 Hz is also applied by the acquisition board.

Acquisition data parameter	
Sampling Frequency	<b>20kHz</b>
dt	<b>1.00E-05</b>
Analogic prefilter	<b>5kHz</b>
Camera fps	<b>1000fps</b>

Table 6.2: Acquisition sensor parameter

## 6.4 Post process

For data post-processing both sensors data and camera videos have been used. In brief way, the acceleration data was used to calculate the displacement, with a double time integration; instead load cell force signal was used to integrate over displacement, calculating the absorbed energy. In order to capture only the specimen impact a video post process was conduct, to correct extrapolate from data the specimen window event. Before start discussing the post process, a block diagram shows better the procedure to achieve the results:

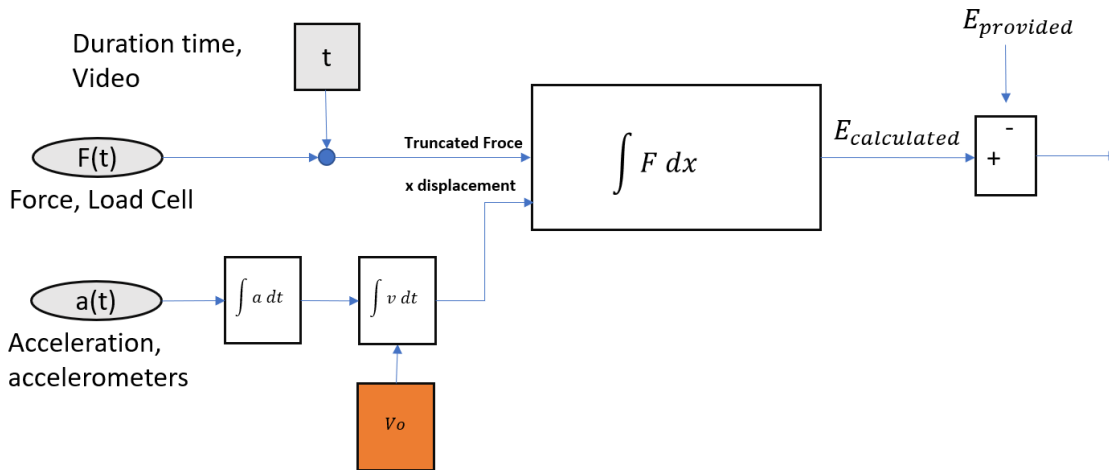


Figure 6.2: Post process block diagram

Starting from the left-hand side: the input data, in time, from accelerometer and load cell sensors are acquired. Thanks to the post process video the duration time event was read. This latter element permits, as already said, to correctly cut the event data window. Proceeding, in order to calculate the energy, the displacement is needed: a mean acceleration is calculated from right and left accelerometers; then, double integrating in time the accelerometer signal, the displacement is calculated. Clearly

the constant integration term  $v_0$  appears in the block diagram, but a better explanation will be presented in the following section. In last block, subtraction between the energy provided and calculated energy.

### 6.4.1 Data post process

A flowchart explain the followed procedure applied on the data. All the post process was achieved using MATLAB software

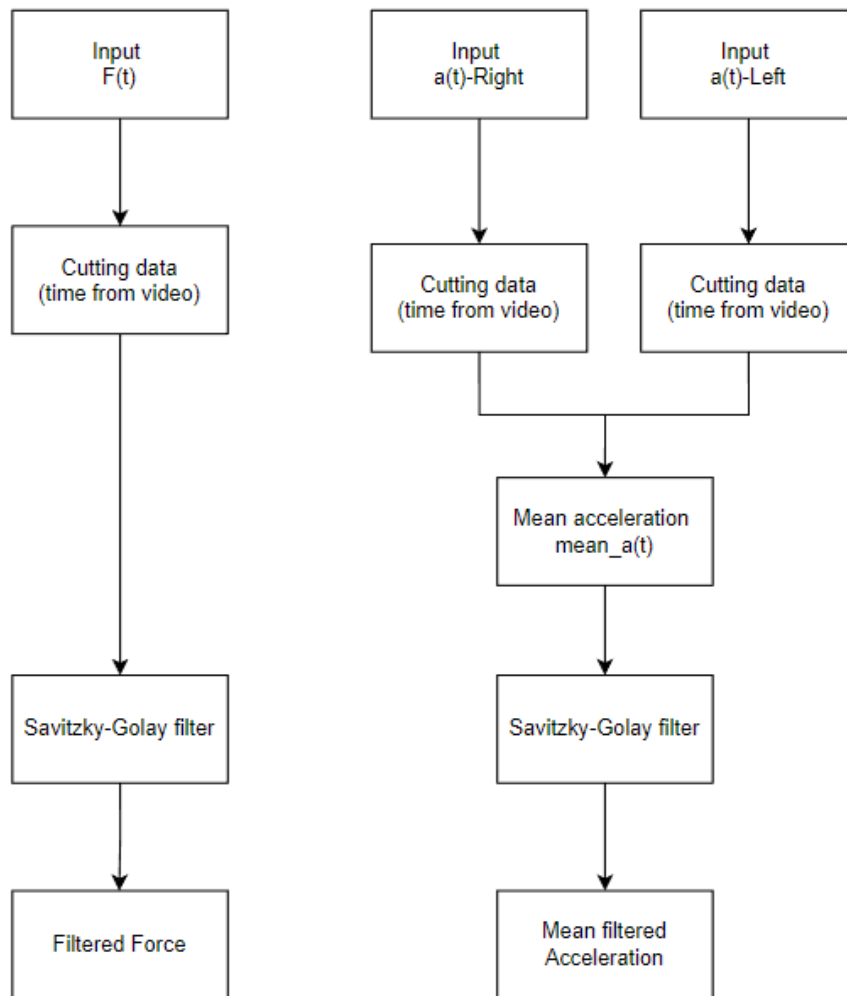


Figure 6.3: Sensors data processing

Speaking about force: incoming signal is stored in an array element with different dimension for each specimen. After, the event window of interest was highlight, cutting

out all useless data, when the specimen finishes absorbing. This was done from post process video. The next step was to filter the signal using Savitzky-Golay with eight order degree and a frame length of 151 points; resulting in a time sample of  $dt = \frac{151 \text{ points}}{20 \text{ kHz}} = 7.5 \text{ ms}$

For the acceleration the procedure was the same, but as already presented, two accelerometers were installed on the hammer head. To have just one signal a point-point mean acceleration have been calculated. In conclusion, before start with integration of the acceleration signal, and to reduce error in the numerical integration, the same force filter Savitzky-Golay have been applied. Again, the size of force and acceleration arrays were the same, because sampled at the same time with same sampling frequency. From this point on the acceleration signal was doubled integrated in time to calculate displacement. In the following figures, data plots will be attached.

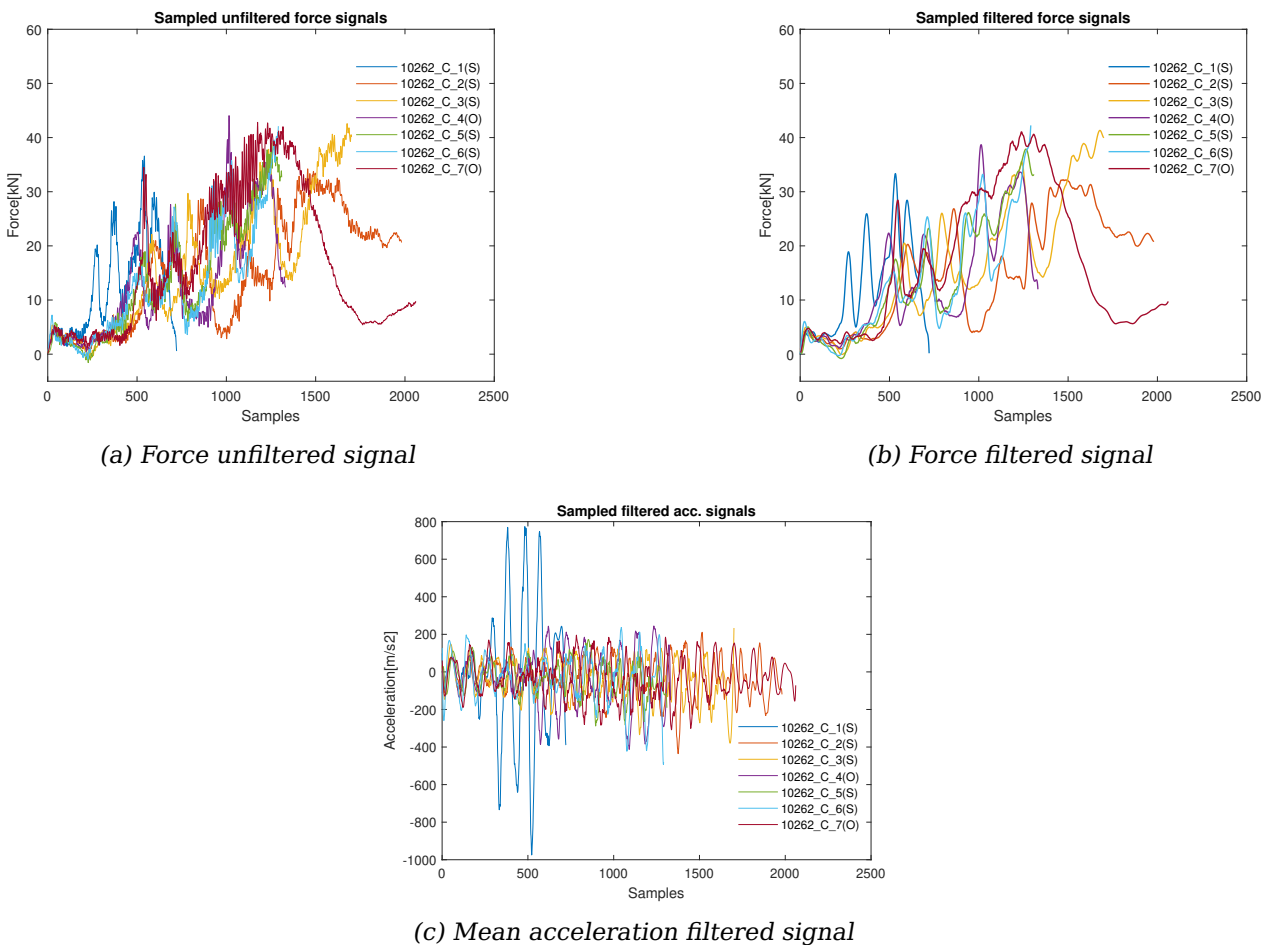


Figure 6.4: Force and acceleration signals

### 6.4.2 Video Post process

Photron FASTCAM Analysis software is used to analyse the crash video. In following figure 6.5

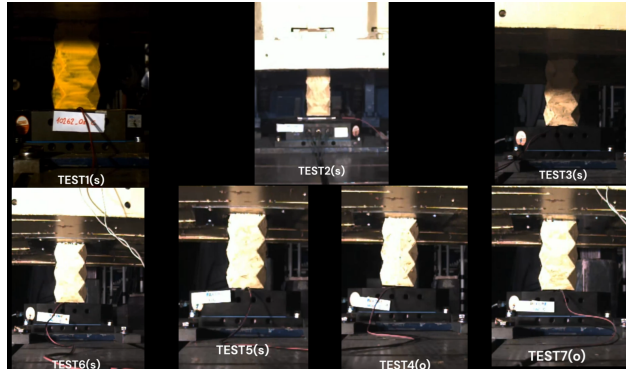


Figure 6.5: Specimen before impact

The main purpose of the video post process is primarily to analyse the dynamic crash behaviour, and secondly, to extrapolate the initial velocity  $v_0$  necessary to integrate the acceleration signal. A problem is found in the camera position, because, it was not perfectly orthogonal to the specimen. This problem was translated into the fact that the software read different velocities for two points on the same rigid body. To solve this problem, and find correctly the right  $v_0$  velocity, three point have been tracked. For sake of simplicity we will call them: **Head point**(blue); **Base point**(red); **Impact point**(teal) in figure 6.6.

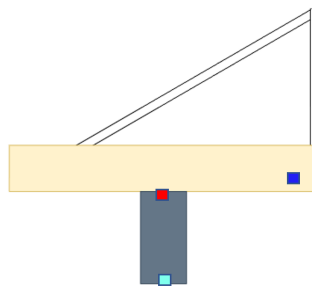


Figure 6.6: Tracked points-video post process

The reference point for post process was the blue points due to the fact that the other ones were lost during the tracking, because of, debris outgoing during crash event. The base and impact points trajectories are good only in the initial part, as soon as the debris coming out during the event. Another problem, was the fact that the

head velocity was major with respect to the theoretical one calculated by the energy conservation principle, with the following formula:

$$v_0 = \sqrt{2gh} \tag{6.3}$$

with  $h$  centre of gravity height.

In conclusion weighted average velocities between head and base point is used. The weight respectively of 0.75 and 0.25 were found reducing the error in diagram 6.2, and not overcoming the maximum permissible displacement (height specimen: 210mm) To summarize the initial velocity at  $t = impacttime$  is:

$$v_0(t = impact) = 0.75V_{HeadPoint} + 0.25V_{BasePoint} \tag{6.4}$$

To check and be sure, that the displacement is correct, a comparison between velocity in time coming from video and integral velocity, have been done and presented in figure 6.7

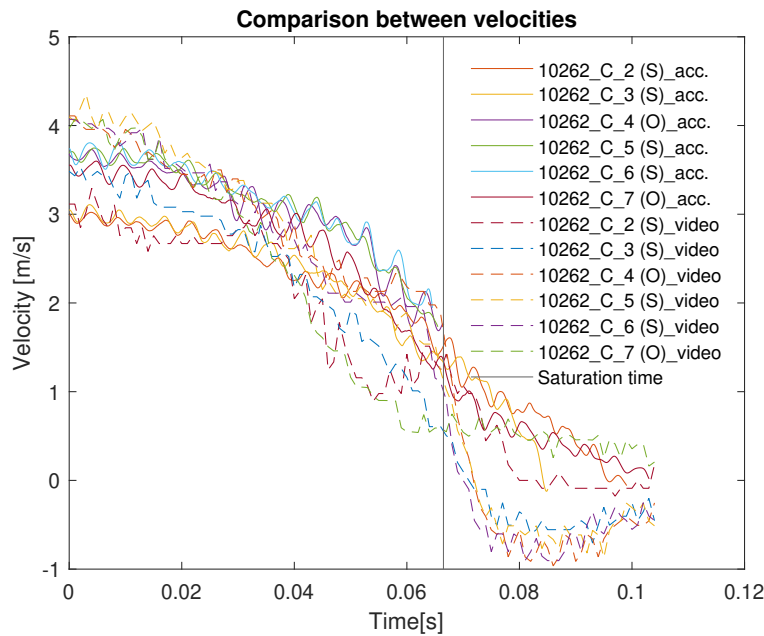


Figure 6.7: Velocity comparison

An important consideration must be does. For some specimen the load cell has reached the saturation limit. To avoid the accounting of the hammer head energy deformation, data, only for these specimens, are cutted out before load cell saturation. The limit is clear in figure 6.7, in fact, a sharp decreasing velocity is visible, highlighted by a vertical black line. To summarize the velocity in time with displacement curves are

presented:

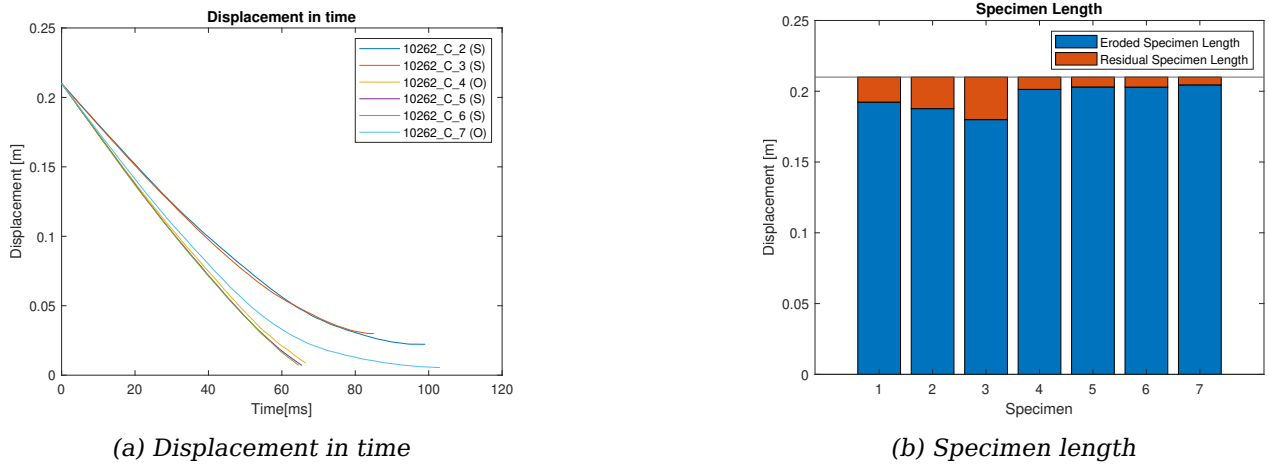


Figure 6.8: Specimen displacement

## 6.5 Post process result and conclusions

In the following section all the useful post process plot and results will be presented. Then, some consideration about breaking dynamics and in conclusion the presentation of acceptability bound to validate the FEM model.

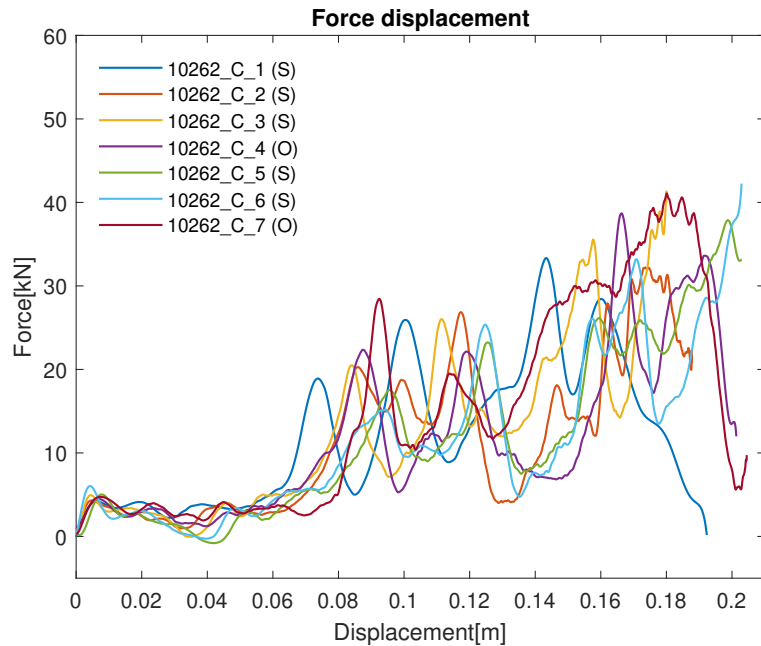


Figure 6.9: Force-displacement curves

As reported in 6.1 not all the specimen were tested with same amount of provided energy.

In consequence of this, only the iso-energetic tested specimen have been used to extrapolate the acceptability bounds and used to validate the FEM model, and analyse the statistics. For sake of clarity, the force displacement curve are reported 6.10

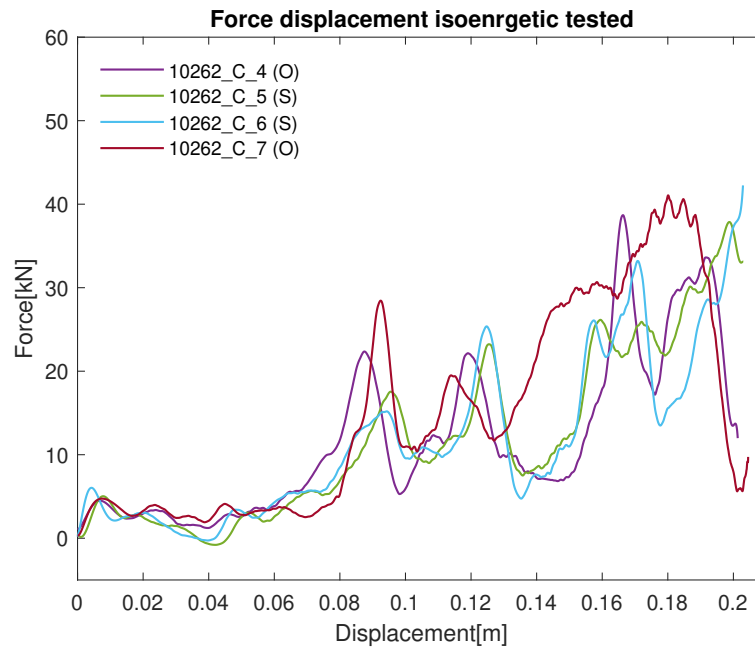


Figure 6.10: Iso-energetic tested specimen force-displacement curves

To remember the specimen were laminated to have 3-6-9 plies for modules 1,2 and 3 respectively. The thickness variation is clearly visible in force curves. A big step is reached when the crash pass from one module to the other. The module with 3 plies is able to quite constantly absorb energy during impact, with a small deceleration of 1.05g. Module 2 and 3 will have, instead, up-down force characteristic. This from the comfort point of view is not good, but is due to an abrupt break of the module which implies this behaviour. Speaking about production method, the overlap one is preferable. The main advantages are depicted in 7th specimen, where a big plateau is reached in last module. The added strip for first production method introduce defects in the bounding plane, where a thickness changing is appreciable.

### 6.5.1 Breakup Dynamics

Already anticipated in the previous section, the breakup dynamics of specimen will be faced. The objective is to investigate the complex crash behaviour; and trying to justify

the out coming results.

To do that, necessary and precious will be the videos coming from cameras. It is important to notice that, the main founded considerations, regards the module one of the crash box, because it is easy to notice the particulars until the debris not obscure the camera. In the following figure 6.11 some crash frame, of just one representative specimen, will be presented.



Figure 6.11: 10262\_C\_05(S)-crash frames

Only specimen 5 will be considered, for simplicity. The first failure point is positioned on the rhomboidal cross-section. This is visible in frame  $t = 5ms$ . Then the crash interests only the first half of module 1 (from  $t = 5$  to  $t = 15$ ). Now the origami shape will fold inside the crash-tube and finally will lose an entire piece, clearly visible in frame  $t = 35$ . For what concern the module 2, the crash behaviour will be the same. Initially the first half module will participate, then a higher force peak is appreciable due to the presence of remaining half module.

In a better way, each module mechanically answer with 2 peaks. Peak number 1 is appreciable in the initial part of the crash, the second one in the second half of the module. The behaviour is quite different only for the module 1, where the second peaks is too small with respect to others module due to a small material thickness.

For other modules starting from frames  $t = 40$  the crash dynamics is not so clear;

especially for module #3 where debris obscure completely the camera view.

### 6.5.2 Acceptability bounds

In order to validate the FEM model presented in the next chapter, some acceptability bounds were being extrapolated from the experimental test. The specimens that participate in the bound extraction will be the follow, because they are tested with the same energy provided:

- 10262\_C\_04(O)
- 10262\_C\_05(S)
- 10262\_C\_06(S)
- 10262\_C\_07(O)

We will call them, iso-energetic tested specimen.

Two specimens for each production method are tested. Intuitively, array size of specimen will not the same, in fact some specimen, spend less or more time to dissipate the energy. The acceptability bounds will be two limits expressed in a force-displacement curve that represents for each displacement point the **MAX** and **min** value, founded interrogating each specimen.

Before doing that, an interpolation in time was necessary, because of different dimensionality array. Then a MATLAB matrix will be created, in which, each column represents the force samples. To extract the limits, for each matrix row, MAX and min values will found. Finally, a displacement vector will be created with the same dimensionality.

In figure 6.12, the acceptability bounds are depicted. On the background a crash box, correctly scaled, was added to better visualize the peaks along the specimen length.

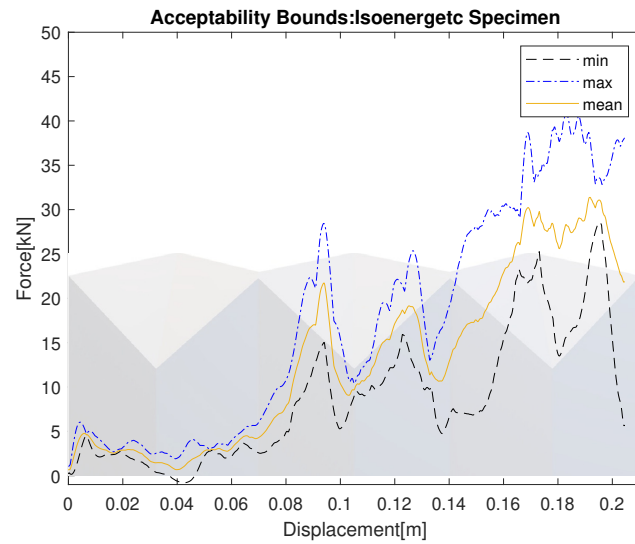


Figure 6.12: Validation acceptability bounds

For iso-energetic specimen, standard deviation was studied and express in a candle force plot. What the figure 6.13 represents, are the variability across the displacement of the force. The "x" symbol will represent the median, instead the upper and lower value of each bar will represent limits on displacement domain. From this plot we can conclude that the module #1 crash behaviour is clearly repeatable, because a small window amplitude is shown. On the contrary proceeding with module #2 and finally module #3, a big amplitude is appreciable. This is justified by the fact that overlap production method absorb more energy, with a particular accent on specimen 7, that showed a big force plateau from 0.14m. This on the contrary reduce results reproducibility and leads to an increment in the window force amplitude.

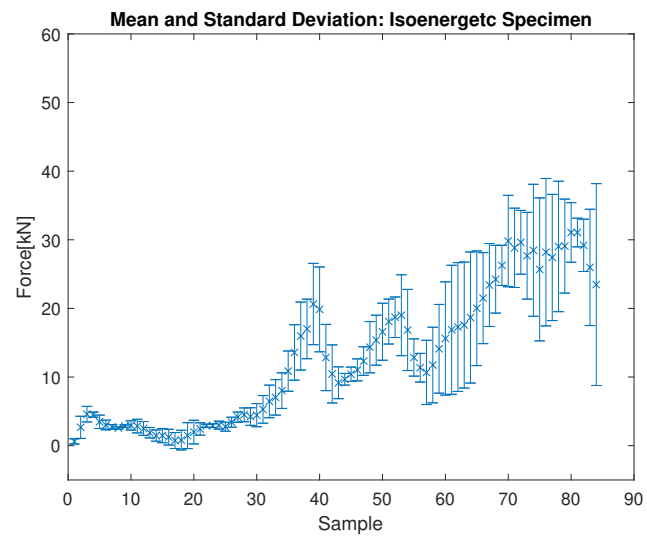


Figure 6.13: Standard deviation candle plot

# Chapter 7

## Numerical Model

In this chapter will be presented the FEM model implemented using LsDyna software. Firstly a summary of the modelling approach used. Then the evaluation results compared with experimental data presented in chapter 6, concluding with a recall on breakup dynamics presented in section 6.5.1.

In chapter 3 two method for modelling the CFRP crash behaviour have been presented. Now we will go deep in detail of the FEM model speaking about the model implementation.

### 7.1 Mesh

To save time and spend less computational energy, the crash box symmetry was taken as advantages. In fact just a quarter of crash box was simulated to fit the model with experimental result. The first operation, after fixed CAD model, was to mesh the component.

Mesh element are needed to discretize geometry. Some hypothesis must be clarified:

- no real fillet radius (3mm) were considered in FEM model
- sled hammer base was not considered

To mesh the quarter crash box model a mesh size of **3mm** have been used. This value was chosen on the base of quality mesh. Starting from the fact that the surfaces of crash box are simple, element with 3mm edge are capable to correctly discretize the geometry.

In addition, for non-linear analysis, the smallest mesh element define the simulation  $dt$ , keeping eye on this parameter.

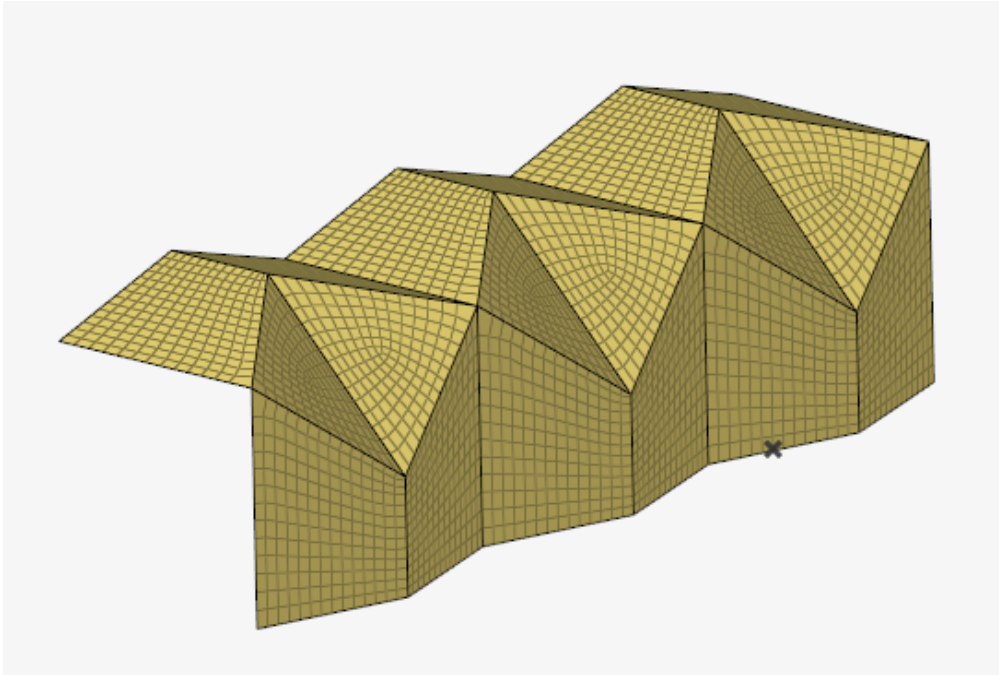


Figure 7.1: Quarter crash box mesh

To mesh the .STP model, drawn in CATIA V5 software, Hypermesh have been used. To evaluate the goodness element mesh, quality index element, already implemented in Hypermesh is used. Thanks to this tool we can easily verify several mesh criteria, attached in the following table 7.1 Finally, an overview parameter called *comp. QI*, globally describe the quality mesh and must be between 0 and 1; otherwise some mesh element fail minimum criteria based on mesh dimension. In table 7.1 all the components are summarized. The presented data are referring to a good mesh threshold criteria, automatically setted by the software.

Finally, the comp. QI will be very close to 0 (ideal mesh) value.

## 7.2 Trigger mesh element

In the preliminary FEM version, the force output simulation found a not real peak force, of roughly the 50% greater than real one. To solve the problem video post-processing have been used. As said before, in chapter 6.5.1 the first crack propagation point is in the rhomboidal section, clearly visible in figure 7.2.

<b>Quality Index Components</b>		
	<b>Element</b>	<b>% element</b>
<b>min size</b>	2992	97.6%
<b>max size</b>	244	8.0%
<b>aspect ratio</b>	64	2.1%
<b>warpage</b>	0	0.0%
<b>skew</b>	1854	60.5%
<b>Jacobian</b>	210	6.8%
<b>max angle quad</b>	914	29.8%
<b>min angle quad</b>	942	30.7%
<b>max angle tria</b>	0	0.0%
<b>min angle tria</b>	0	0.0%
<b>taper</b>	47	1.5%
<b>comp. QI</b>	<b>0.06</b>	

Table 7.1: Mesh quality index components

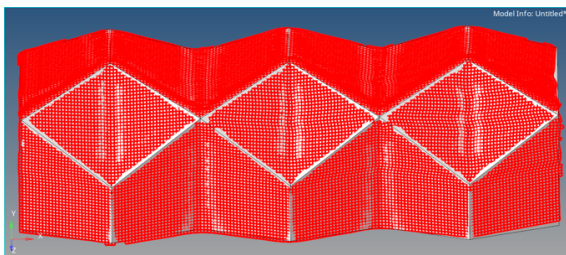


Figure 7.2: First failure point - crash box

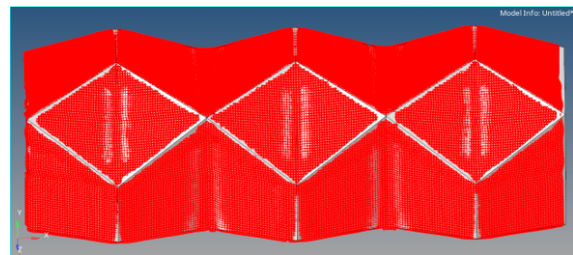
To solve the force peaks problem, and justify the unusual trigger position, comes to help the kinematic drape tools implemented in Hypermesh. The guidelines software suggested for twill carbon fiber cloth to simulate separately  $0^\circ$  and  $90^\circ$  plies. The output from kinematic drape are:

- simulation of plies placement
- shear angle parameter

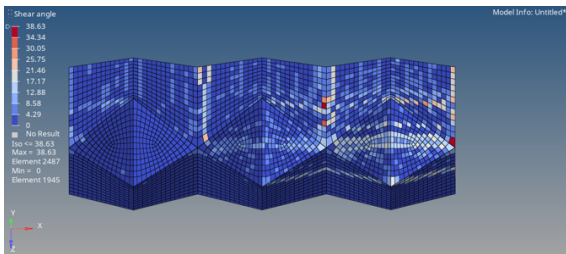
In following figure two representative plies were implemented in Hypermesh tool, to see where defects intensify. What is important to notice, are regarding the image 7.3a: in the diagonal zone an abnormal ply deposition is forecasted. This is confirmed seeing the shear angle parameter in picture 7.3d, that describe how much the ply is distorted after the lamination with respect to the original direction.



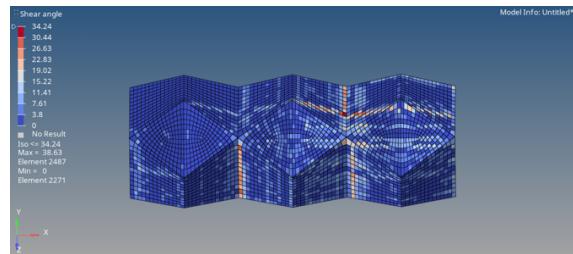
(a) drape simulation - ply 1



(b) drape simulation - ply 2



(c) 0°twill ply



(d) 90°twill ply

Figure 7.3: Kinematic drape output

From now, we can translate the defect into FEM model. The idea was to penalize some mesh element in order to induce here before the crash. In figure 7.4 implemented trigger FEM model. To penalize the trigger elements *SOFT* and *DFAILC* was manually tuned.

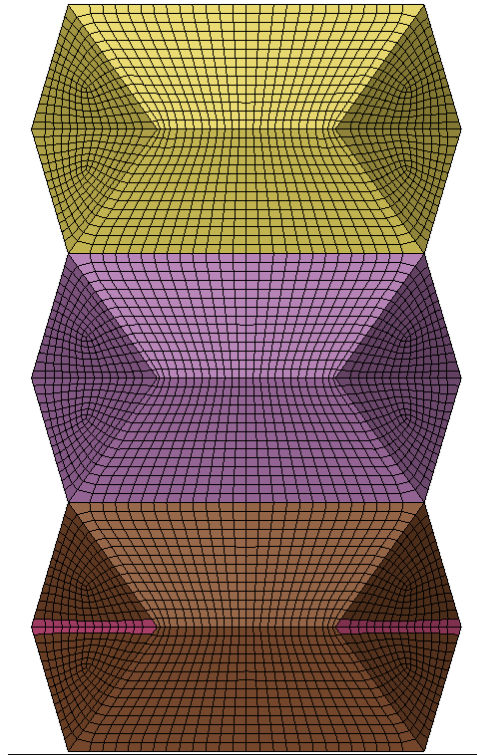


Figure 7.4: First failure point - crash box

The results not only will be translated in reducing the first abnormal force peak but also having the same crash real behaviour in the FEM model. Evaluation and comparison between FEM model and experimental data are faced in section.

### 7.3 Shell Model

In chapter 3 the shell modelling approach is introduced. The material card used for model shell is MAT54, already presented in chapter 4.

The shell version discretizes carbon fiber plies only with no thickness element using ELFORM16 regarding EQ.16: Fully integrated shell element.

Suggested by LsDyna guide HOURGLASS control energy (type 8) is used. The hourglass energy is an artificial-added energy to stabilize the simulation.

To create each plies PART-COMPOSITE element were defined, imposing the  $0^\circ$  orientation plies. For all FEM model using carbon fiber the main material direction must be specified. In our case, due to geometry orientation, the x direction become the carbon fiber direction.

## 7.4 Combined Model (Shell+Cohesive)

For what concern the so called combined model, we have two different modelling. Remembering, the IA validation specimen were laminated with the following layup: 3-6-9. Having a post cure ply thickness of 0.23mm, the final component will result in: 0.69-1.38-2.07 mm. Main behaviour in carbon fiber crash component, when thickness increase, is delamination effect. This is appreciable when the component thickness is big enough. For module #1 where the component measure 0.69 mm, shell modelling is sufficient to capture correctly the energy absorbing and force output signal. The idea was to evaluate a combined model with shell only for the first module and then using cohesive solid element for module #2 and #3. To evaluate the correct cohesive approach, as seen in chapter 3, several FEM versions were tested to correctly fit experimental results. The final configuration express as rule of tomb will be the following:

$$t_{cohesive} = 25\%t_{plies} \quad (7.1)$$

where  $t$  indicates the thickness. To summarize, in table 7.2 all the utilized value.

	<b>Plies</b>	<b>CFRP thickness [mm]</b>	<b>Cohesive thickness [mm]</b>
<b>Module #1</b>	3	0.69	-
<b>Module #2</b>	6	1.38	0.345
<b>Module #3</b>	9	2.07	0.5175

*Table 7.2: Cohesive thickness*

### 7.4.1 Cohesive element implementation

LsDyna software guide suggests different method to build cohesive element. For our purpose this idea was followed: starting from shell mesh element, the cohesive solid part must be share the same node. To be secure on that the solid part was created by a 2d mesh offset took as reference. Now a shell face extraction from solid part was done. To better visualize a small figure 7.5 depicts the operation.

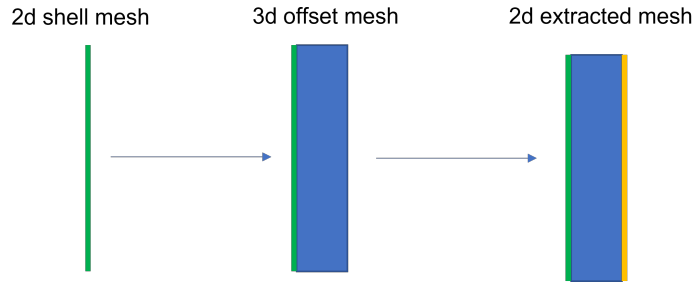


Figure 7.5: Cohesive implementation

Finally, the quarter combined model is attached in figure 7.6. What is important to notice, is the laminate growth direction. Outer plies and inner plies growth opposite to the cohesive solid part.

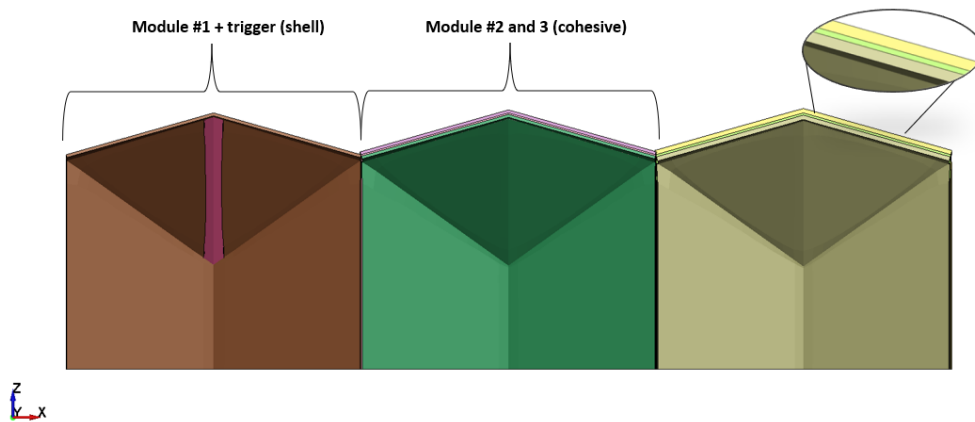


Figure 7.6: Combined model

## 7.5 Boundary Conditions

To better take advantages of crash box symmetry, just one quarter was simulated. To correctly simulate it the following boundary condition were applied: On left side figure 7.6 is present the system of reference.

- symmetry along plane  $xy$
- symmetry along plane  $xz$

Boundary not permits the translation, respectively, along the y and z axis, and rotation around x one. For simulation purpose the interaction between base specimen and sled hammer was not accounted.

## 7.6 FEM results

In following section the results of fem model will be firstly discussed. Then, a comparison between experimental results and numerical model output, to access the goodness of the model. In addition, also a dynamic crash behaviour result will be accessed, still comparing FEM and real test.

### 7.6.1 Force displacement curve - shell model

In figure 7.7 force-displacement curve regarding shell model will be depicted. To evaluate the validity of models also the experimental acceptability bounds are plotted.

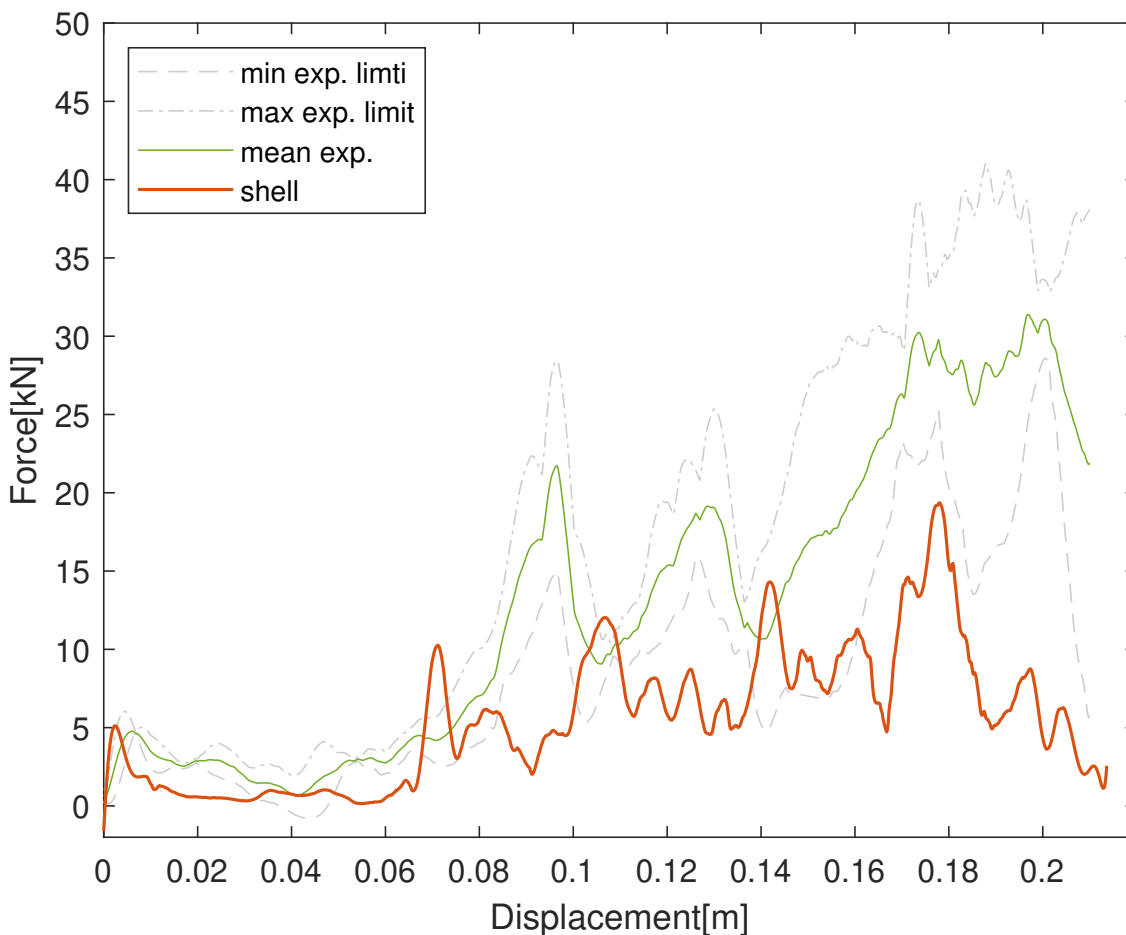


Figure 7.7: Force displacement curve - shell model

As said before, in model is implemented trigger element. In a first view, the shell model does not perform bad. In terms of characteristic shape this model is able to

correctly predict the general behaviour.

Proceeding with order: in module #1 first peak force is correctly intercepted, thanks to trigger; a slight difference is in the rigidity response. After the initial part, crash proceeds in a good way, the force output curve for module #1 is in acceptability bounds. Also in terms of absorbed energy (seen as the subtended area). From module #2 the specimen thickness become considerable. Now the shell model will not be able to lie in bounds limits, because fails, not seeing, delamination effect, that become predominant when carbon fiber thickness increase. The offset from experimental curve increase in module #3, for the same principle explained for the previous one.

Although the shell model is not able to predict the behaviour, when the thickness increase, it will be useful for the first part design, as preliminary study.

### 7.6.2 Force displacement curve - combined model

In the same shell way, the force displacement curve regarding combined model will be, here, discussed.

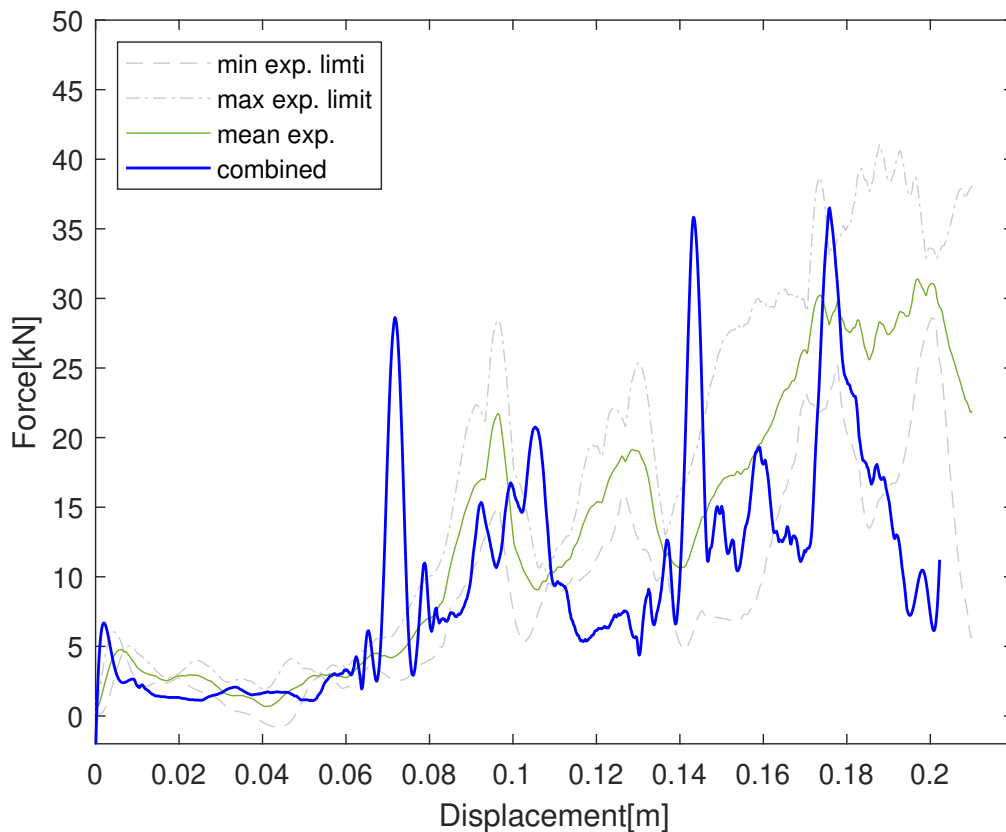


Figure 7.8: Force displacement curve - combined model

For module #1 the same, previous presented, formulation have been used, because shell element are able, for this laminate thickness to correctly behaves. What is important to notice, is the capacity, with respect to previous model, to capture in module #2 #3 the crash carbon fiber delamination effect. Remembering, carbon fibers show several failure mode, but the delamination has the majority. A particular attention at displacement point  $d = 0.07m$  the transition between shell and cohesive modelling results in a strange spike force, resulting in an “anticipated” specimen response with respect to experimental results. An important model achievement is regarding the correct forecasting of peak force and so the maximum deceleration picked with small error.

### 7.6.3 Numerical model error

In the following section FEM model and experimental results will be put in comparison to evaluate the goodness numerical model.

$$MSE_{Force} = MEAN [(F_{Experimental} - F_{FEM})^2] \quad (7.2)$$

$$MAE_{Force} = MEAN [| (F_{Experimental} - F_{FEM}) |] \quad (7.3)$$

$$RMSE_{Force} = \sqrt{MSE} \quad (7.4)$$

$$\epsilon_{Energy} = \frac{E_{Experimental} - E_{FEM}}{E_{Experimental}} * 100 \quad (7.5)$$

Where:

- MSE: Mean Square Error
- MSE: Mean Absolute Error
- MSE: Root Mean Square Error
- $\epsilon_{Energy}$  = Relative Energy Error

	Shell Model	Combined Model
MSE [kN]	109.9	72.08
MAE [kN <sup>2</sup> ]	7.75	5.99
RMSE [kN]	10.48	8.49
$\epsilon_{ENERGY}$ %	56.60	28.79

Table 7.3: Numerical model performances

In table 7.3 all the numerical performance parameter are summarized. In a predictable way, also seeing the displacement - force curves, the combined model performs better with respect to the shell one. Interesting are the evaluated error. Globally the errors are quite big. This effect is because of the misalignment in displacement domain, discussed before. In crash event fundamental parameters are: mean deceleration, max deceleration, energy absorption. The deceleration is related to force by Newton law. Now the deceleration information are summarized 7.4. After calculating the max and mean quantity will be evaluated the error with respect to real test in peaks force characteristic points as shown in figure 7.10.

	<b>Real</b>	<b>FEM</b>
<b>Max deceleration [g]</b>	8.7	7.8
<b>Mean deceleration [g]</b>	3.7	2.1

Table 7.4: Max and mean acc. comparison

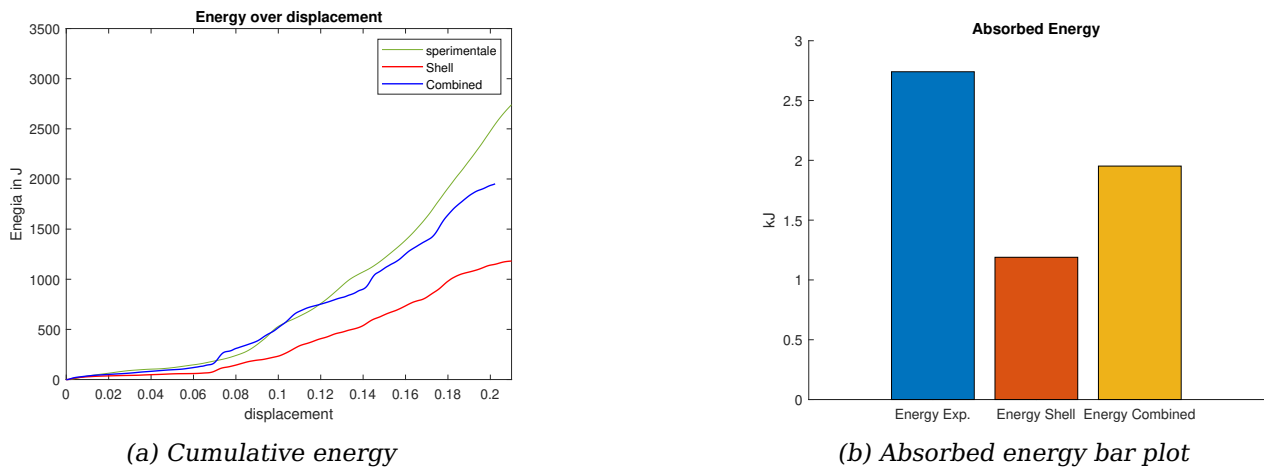


Figure 7.9: Energy absorption

Seeing the figure 7.9a it is appreciable the cumulative energy absorbed in displacement domain. In the first two, of three, crash box modules, the curve representing the cumulative force integral over displacement, is roughly coincident. Concluding that the model is able to correctly capture the absorbing energy.

The green curve will be the average cumulative energy coming from experimental curves.

Now to demonstrate the validity of the FEM model an analysis on some characteristic points will be conducted. Will be used the following point notation. Subscript "e" will

represent *experimental* curve points, instead, subscript “f” will represent *FEM* curve points.

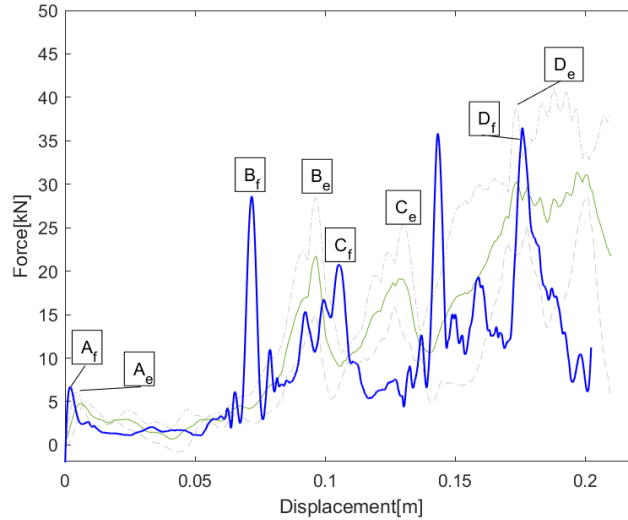


Figure 7.10: Characteristic points

All the numerical values are summarized in table 7.5. There, appears also the FEM error calculated with respect to real. The maximum error will be on the first point with 10.78% higher. By the way, the important error is regarding the max acceleration point, because can cause major injuries; so the error in the most sensible point will be of 5.86%. Model is able to predict in a very reliable way the max acceleration value.

Characteristic Points							
Forces [kN]							
<b>A<sub>f</sub></b>	6.7	<b>B<sub>f</sub></b>	28.6	<b>C<sub>f</sub></b>	20.7	<b>D<sub>f</sub></b>	38.7
<b>A<sub>e</sub></b>	6.0	<b>B<sub>e</sub></b>	28.4	<b>C<sub>e</sub></b>	25.4	<b>D<sub>e</sub></b>	36.5
<b>FEM error</b>	10.78%		0.67%		-18.44%		5.86%

Table 7.5: Force numerical values - characteristic points

In literature, another important performance parameter is the so-called SEA: Specific Energy Absorption. In the following the equation is reported.

$$SEA = \frac{E_{absorbed}}{\rho A \delta} = \frac{\int F dx}{\rho A \delta} \quad (7.6)$$

where  $E_{absorbed}$  is the absorbed energy, calculated integrating the force (F) in displacement (dx); A is the cross-section, and  $\delta$  the crashed specimen length. comparison

	SEA (on module 1) [KJ/kg]	SEA (on module 2) [KJ/kg]	SEA (on module 3) [KJ/kg]
<b>Experimental</b>	25.53	61.28	76.70
<b>Numerical</b>	23.60	50.52	48.49

Table 7.6: Specific Energy Absorption for each crash box module

between experimental and numerical SEA is summarized in table 7.6 Due to the different layout on each module, the SEA have been calculated for module 1, 2 and 3 separately, having different cross section. The SEA value are comparable for modules 1 and 2. Instead, for last module a high difference of around 24kJ/kg are quite high.

### 7.6.4 crash behaviour

Now an overview about the crash dynamics. In the following, a comparison between the real and FEM model images. As said in chapter concerning the crash analysis image, main conclusion are related to module #1. The FEM model, thanks to trigger element to have the same progression. The FEM model images are an important tool to know about effect in module #2 and #3, when the camera become unable to see due to debris during the event. In Figure 7.11 are presented the images in time with a time step of 5ms for sake of simplicity.

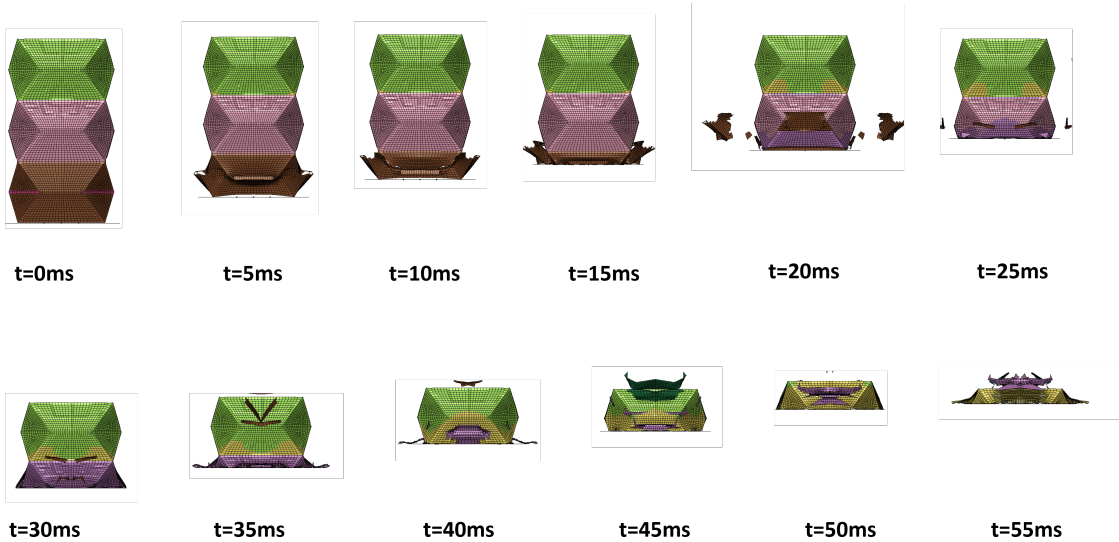


Figure 7.11: crash frames numerical model

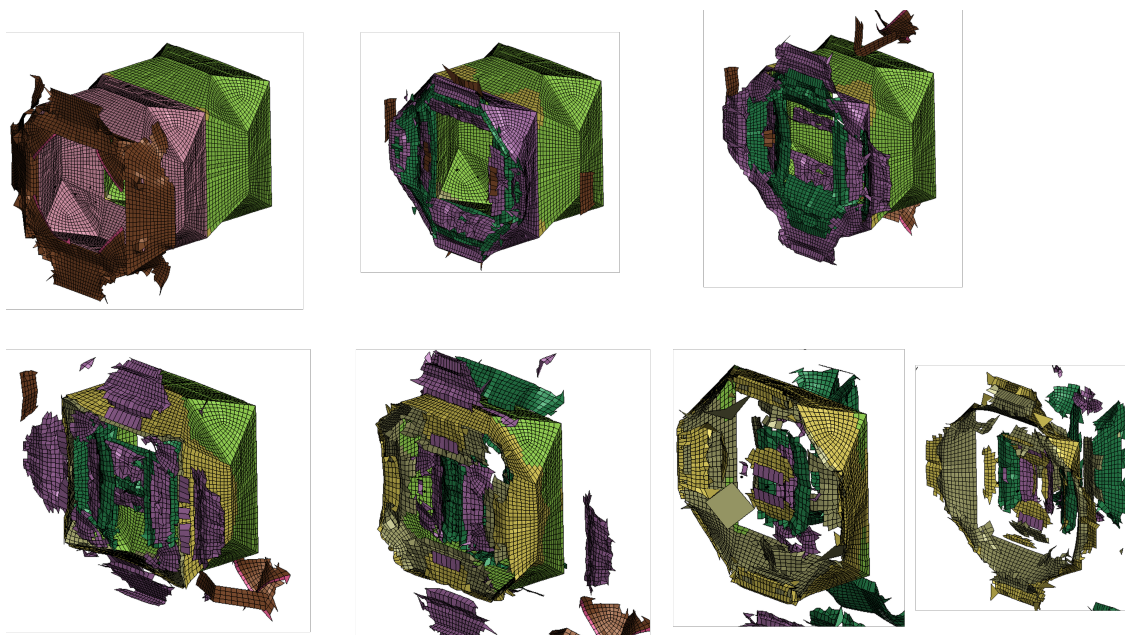


Figure 7.12: Delamination frames numerical model

Now the force displacement curve will be linked to dynamics of the event. To better see the effect in the already presented F-d curve will be attached some frames.

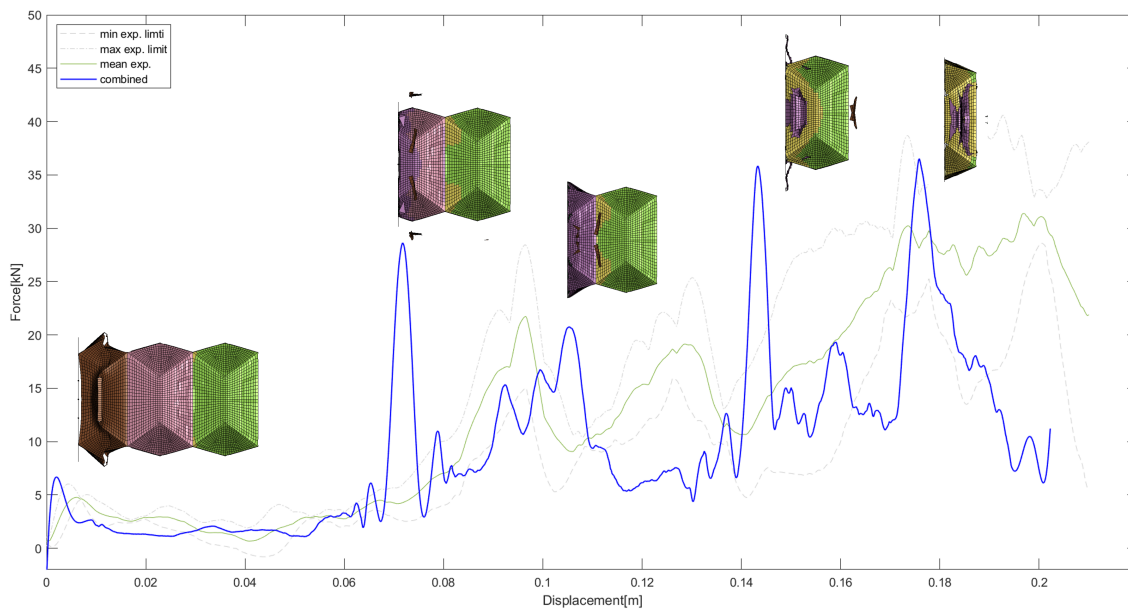


Figure 7.13: Force displacement interpretation

The first peak force is due to the failure in rhomboidal cross-section, like the real test. The first half module will participate in the force signal. The second peak is due

to the second half module, with an unfolding of the origami module outside crash box, clearly visible in 7.12. The principle governing the dynamics in module #2 and #3 is quite different. The crack propagates from the beginning of the module, followed by an inside folding of the origami shape. Now the delamination failure have the main contribution. In isometric view frames, are visible the carbon fiber plies incurring delamination. The two characteristics are misaligned in displacement domain, but although this, the displacements window between the two peaks are correct.



# Chapter 8

## IA final configuration

The main thesis goal is to realize a component able to absorb the right amount of energy prescribed by Formula Student rules, submitting not only the dimensional needs presented in chapter 2; but respecting, all the force and acceleration requirements. The seven tested experimentally specimen were not able to absorb all the energy (7350J) but they were used as a reference to correctly tune numerical model. In this chapter we will go head, to find the correct layup compliant to the rules, tacking fixed the IA geometry. Regarding the geometry, it has been left the same for production reason. The procedure to find the final target configuration was done manually. When we speak about composites component the main design phase is regarding the layup optimization. Contrary to the classic way of thinking, design with carbon fiber part means also study the layup and fiber orientation.

Some preliminary specifications are necessary: now we are not only interested to impact attenuator structure, but we take a look also to **AIP** (Anti Intrusion Plate) contribution, all attached to fixture (see figure 2.2).

The AIP and the fixture element are realized with a sandwich structure. The 20mm thick aluminium core is in between several carbon fiber plies.

### 8.1 Final layup

The final configuration will be:

**5 - 7 - 10**

As already explained the above notation means that the crash box is composed by three modules with the following ply each:

**MODULE 1: 5 plies**

**MODULE 2: 7 plies**  
**MODULE 3: 10 plies**

In order to gradually absorb the energy, resulting in a growing deceleration, the crash box has different layup configuration on each module

A manual process, to achieve the acceleration and energy target, was used. The carbon fiber is a high strength material. This is at the same time a plus in terms of capacity, from the material point of view, to absorb high energy. On the contrary, there is an equivalency between high strength and deceleration. To solve the problem, the origami structure combined this two keys aspect. In addition, thanks to the progressive growing of the plies, the deceleration will be maintained under control.

## 8.2 Force displacement curve

In the following section, force - displacement curve of the final target impact attenuator structure will be depicted.

The final structure, previously described, is composed by three components:

**FIXTURE STRUCTURE:** simulating monocoque

**AIP:** anti intrusion plate

**IA:** impact attenuator

To simulate the response of the sandwich panel, material card MAT26 have been used, in [15], authors characterize a honeycomb panel, following the ASTM D365, in case of crash condition. The tested honeycomb was: 4.5-5052-1/8, indicating the density of 4.5 pound (ca. 2 kg) per cubic feet, with Aluminium series 5052 and a cell dimension of 1/8 of inches. In our AIP structure a 6.1-5052-1/8 honeycomb have been used. Now the final FEM target model is presented. As usual, component symmetry has been exploited. The presented image represents only the half structure (IA + AIP), out coming from numerical model simulation.

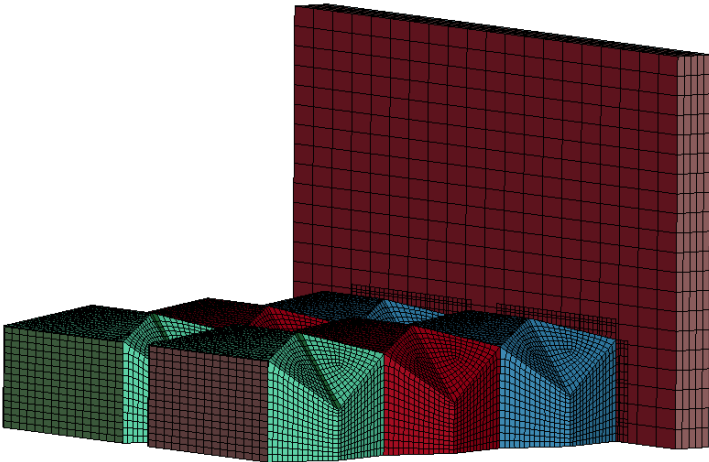


Figure 8.1: Target FEM model-half structure

As visible in 8.1, the impact attenuator structure has a closed frontal cross-section, to limits the penetration of a sharp object, as mentioned in [2].

The force displacement curve is now attached, this referring to the complete structure and not only the half:

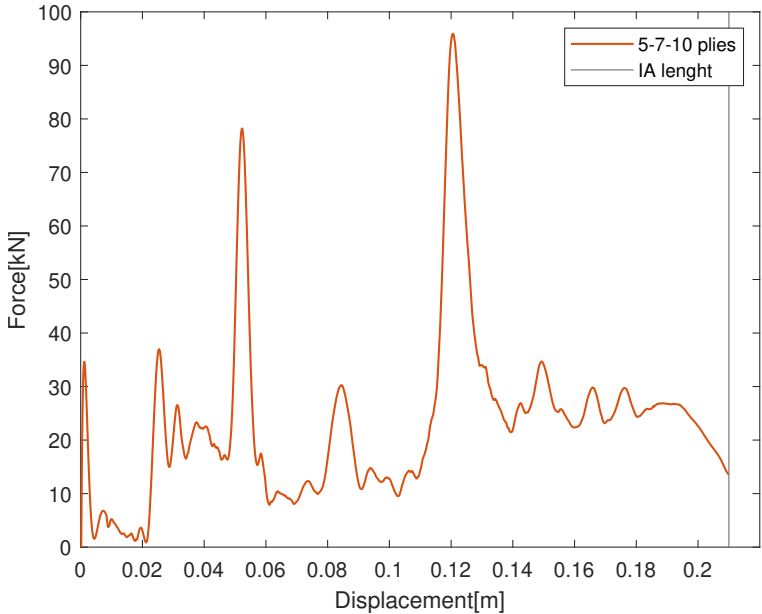


Figure 8.2: force displacement curve - final setup

### 8.3 Performances indicator and comparison with previous attenuator

Now some performance indicator on the crash box will be analysed. In dynamics crash event the main parameter useful to maintain under control will be: the mean acceleration, and the total absorbed energy. The goal is to minimize the former and maximize the latter. In addition, also the maximum deceleration value is critical in the design phase, to limit the injuries.

The new structure absorbs an energy content of **7400J** respecting the Formula Student Rules, with an average deceleration of **7.9G** with a peak of **32G**.

Before start with the performances evaluation, a brief summary about previous attenuator structure is necessary. In picture 8.3, the hybrid Al + carbon fiber attenuator is depicted. The attenuator was composed by three aluminium honeycomb blocks (Al 5052 5.2 - 1/4) with a high of 80mm each. The blocks are interspersed by a carbon fiber plate positioned to avoid collapsing and instabilities in the honeycomb structure. The interface between honeycomb and carbon fiber plate is guaranteed by structural epoxy glue PLEXUS.



*Figure 8.3: Previous attenuator structure*

In table 8.1 a performances comparison between old attenuator and new one are summarized:

	<b>Old attenuator</b>	<b>New attenuator</b>
<b>Weight [kg]</b>	0.55	0.474
<b>Max acc [g]</b>	25	32
<b>Mean acc [g]</b>	10	7.9
<b>Energy [kJ]</b>	7.38	7.4

Table 8.1: Old and new attenuator performances

The new carbon fiber attenuator has better performances: in terms of weight, there will be a saving of 14% with respect to the previous Al structure. In addition, the mean deceleration is 21% less, passing from 10g to 7.9g, due to the fact that the carbon fiber attenuator have a better gradually absorption of the energy. The oldest version responds rapidly with a constant high force. The main drawback is regarding the maximum deceleration peak of 32g for carbon fiber crash box, remembering that the maximum permissible limit is of 40g, including the non-crushable object mentioned in chapter 2.

In the following plot 8.4 all the above parameters are summarized to graphically keep in mind the mentioned values. A four dimensional spider plot indicates the following categories, one for each axis: weight; max acceleration; mean acceleration; and absorbed energy. The values are referred to table 8.1

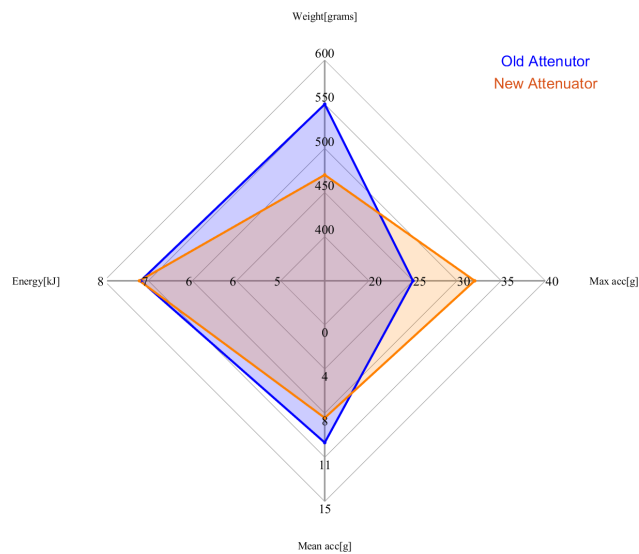


Figure 8.4: Performances comparison - old and new attenuator structure



# Chapter 9

## Conclusions

This thesis presents a study on an origami-shaped composite structure designed, produced, and tested as a crash absorber for a Formula Student race car. The choice of an origami structure was motivated by its potential to enhance the energy absorption capabilities of composite materials. The thesis covers various aspects, including material characterization, impact attenuator geometry, specimen production, experimental tests, and a numerical model of the crash box.

The results demonstrate that the origami-shaped crash box fulfils the requirements outlined in the Formula Student rules while exhibiting efficient energy absorption. This confirms the viability and advantages of incorporating origami structures to enhance the crashworthiness of composite material structures. The findings also offer valuable insights for future research in this domain.

Based on the numerical results, the final configuration of the impact attenuator was evaluated using performance indicators such as energy absorbed, final weight, maximum acceleration, and average acceleration. A comparison with the previous honeycomb structure revealed that the new origami-shaped attenuator delivers superior energy absorption efficiency and reduced mass. Consequently, the origami-shaped impact attenuator proves to be a suitable solution that meets the safety requirements of the Formula Student race car.

Moreover, the new carbon fiber attenuator outperforms the previous aluminium (Al) structure in terms of weight, resulting in a 14% weight reduction. Additionally, the average deceleration is 21% lower, decreasing from 10g to 7.9g. This improvement can be attributed to the carbon fiber attenuator's gradual energy absorption characteristics.

Although the final layout was optimized in terms of carbon fiber arrangement, the project also highlights the potential for investigating the origami geometry parameters. This avenue of exploration presents a valuable alternative solution in the automotive market's passive safety systems domain.



# Bibliography

- [1] A. Ciampaglia, D. Fiumarella, C. Boursier Niutta, R. Ciardiello, and G. Belingardi, "Impact response of an origami-shaped composite crash box: Experimental analysis and numerical optimization," *Composite Structures*, vol. 256, p. 113 093, Jan. 2021. DOI: [10.1016/j.compstruct.2020.113093](https://doi.org/10.1016/j.compstruct.2020.113093).
- [2] *Formula student rules*. [Online]. Available: [https://www.formulastudent.de/fileadmin/user\\_upload/all/2023/rules/FS-Rules\\_2023\\_v1.1.pdf](https://www.formulastudent.de/fileadmin/user_upload/all/2023/rules/FS-Rules_2023_v1.1.pdf).
- [3] S. Boria, G. Belingardi, D. Fiumarella, and A. Scattina, "Experimental crushing analysis of thermoplastic and hybrid composites," *Composite Structures*, vol. 226, p. 111 241, Oct. 2019. DOI: [10.1016/j.compstruct.2019.111241](https://doi.org/10.1016/j.compstruct.2019.111241).
- [4] Jianfeng Wang, Na Yang, Jinghui Zhao, *et al.*, "Design and experimental verification of composite impact attenuator for racing vehicles," *Composite Structures*, vol. 141, pp. 39–49, May 2016. DOI: [10.1016/j.compstruct.2016.01.013](https://doi.org/10.1016/j.compstruct.2016.01.013).
- [5] Jovan Obradovic, Simonetta Boria, and Giovanni Belingardi, "Lightweight design and crash analysis of composite frontal impact energy absorbing structures," *Composite Structures*, vol. 94, pp. 423–430, Jan. 2012. DOI: [10.1016/j.compstruct.2011.08.005](https://doi.org/10.1016/j.compstruct.2011.08.005).
- [6] Devon Hartlen, John Montesano, and Duane Cronin, *6th international ls-dyna® users conference cohesive zone modeling of adhesively bonded interfaces: The effect of adherend geometry, element selection, and loading condition*, 2020. [Online]. Available: <https://www.dynalook.com/conferences/16th-international-ls-dyna-conference/modeling-t11-1/t11-1-b-modeling-009.pdf> (visited on 06/02/2023).
- [7] Ravin Garg, Iman Babaei, Davide Salvatore Paolino, *et al.*, "Predicting composite component behavior using element level crashworthiness tests, finite element analysis and automated parametric identification," *Materials*, vol. 13, p. 4501, Oct. 2020. DOI: [10.3390/ma13204501](https://doi.org/10.3390/ma13204501). (visited on 05/08/2022).

## BIBLIOGRAPHY

---

- [8] Iman Hosseinpour Babaei, Ravin J Garg, Lorenzo Vigna, *et al.*, “Newly developed anti-buckling fixture to assess the in-plane crashworthiness of flat composite specimens,” vol. 10, pp. 7797–7797, Nov. 2020. DOI: [10.3390/app10217797](https://doi.org/10.3390/app10217797). (visited on 06/03/2023).
- [9] *Standard test method for tensile properties of polymer matrix composite materials*, [www.astm.org](http://www.astm.org). [Online]. Available: [https://www.astm.org/d3039\\_d3039m-08.html](https://www.astm.org/d3039_d3039m-08.html).
- [10] *Standard test method for compressive properties of polymer matrix composite materials with unsupported gage section by shear loading*, [www.astm.org](http://www.astm.org). [Online]. Available: [https://www.astm.org/d3410\\_d3410m-16e01.html](https://www.astm.org/d3410_d3410m-16e01.html).
- [11] Aleksandr Cherniaev, John Montesano, and Clifford Butcher, *5th international ls-dyna @ users conference modeling the axial crush response of cfrp tubes using mat054, mat058 and mat262 in ls-dyna @*, 2018. [Online]. Available: <https://www.dynalook.com/conferences/15th-international-ls-dyna-conference/composites/modeling-the-axial-crush-response-of-cfrp-tubes-using-mat054-mat058-and-mat262-in-ls-dyna-r>.
- [12] *Ls-dyna® aerospace working group modeling guidelines document*. [Online]. Available: [https://www.predictiveengineering.com/sites/default/files/MGD\\_v21-1.pdf](https://www.predictiveengineering.com/sites/default/files/MGD_v21-1.pdf) (visited on 12/10/2022).
- [13] Lin Yuan, Haoyuan Shi, Jiayao Ma, and Zhong You, “Quasi-static impact of origami crash boxes with various profiles,” *Thin-Walled Structures*, vol. 141, pp. 435–446, Aug. 2019. DOI: [10.1016/j.tws.2019.04.028](https://doi.org/10.1016/j.tws.2019.04.028).
- [14] A Ciampaglia, D Fiumarella, and C Boursier Niutta, *Metodologia per la previsione del comportamento a schiacciamento di una struttura origami mediante intelligenza artificiale*.
- [15] Paolo Feraboli, Francesco Deleo, Bonnie Wade, *et al.*, “Predictive modeling of an energy-absorbing sandwich structural concept using the building block approach,” *Composites Part A: Applied Science and Manufacturing*, vol. 41, pp. 774–786, Jun. 2010. DOI: [10.1016/j.compositesa.2010.02.012](https://doi.org/10.1016/j.compositesa.2010.02.012). [Online]. Available: <https://www.sciencedirect.com/science/article/pii/S1359835X10000692> (visited on 01/17/2022).